Geochemical, Sr–Nd–Pb and zircon U–Pb–Hf isotopic constraints on the Late Carboniferous back-arc basin basalts from the Chengjisihanshan Formation in West Junggar, NW China

Author for correspondence: Yongjun Li, Email: yongjunl@chd.edu.cn

Qian Zhi[1] , Yongjun Li[1,2], Fenghao Duan[1,3], Lili Tong[1,2], Jun Chen[4], Junbao Gao[4] and Rongguang Chen[4]

[1]School of Earth Science and Resources, Chang'an University, Xi'an 710054, PR China; [2]Key Laboratory for the Study of Focused Magmatism and Giant Ore Deposits, MNR, Xi'an 710054, PR China; [3]State Key Laboratory of Nuclear Resources and Environment, East China University of Technology, Nanchang 330013, PR China and [4]No.1 Geological Survey Party, Xinjiang Bureau of Geology and Mineral Resource Exploration, Changji 831100, PR China

Abstract

West Junggar in the southwestern Central Asian Orogenic Belt is a critical area for the study of the Junggar oceanic basin and may also reveal tectonic evolutionary events before the final closure of the Palaeo-Asian Ocean. The sedimentary formations and paragenetic associations of the Upper Carboniferous Chengjisihanshan Formation in southern West Junggar jointly reveal a back-arc basin setting with zircon U–Pb ages of 313–310 Ma for the basaltic rocks. Geochemically, the basaltic rocks are tholeiitic with low SiO_2 (47.76–52.06 wt %) and K_2O (0.05–0.74 wt %) but high MgO (6.55–7.68 wt %) contents and Mg no. (52.9–58.9) values. They display slightly flat rare earth element patterns with weak positive Eu anomalies, and show enrichments in large ion lithophile elements relative to high field strength elements with negative Nb and Ta anomalies, exhibiting both N-MORB-like and arc-like signatures, similar to the back-arc basin basalt from the Mariana Trough. The high positive zircon εHf(t) and bulk εNd(t) values as well as high initial Pb isotopes, together with relatively high Sm/Yb and slightly low Th/Ta ratios imply a depleted spinel lherzolitic mantle source metasomatized by slab-derived fluids. The field and geochemical data jointly suggest that the volcanic rocks within the Chengjisihanshan Formation were formed in an intra-oceanic back-arc basin above the northwestward subduction of the Junggar oceanic lithosphere in southern West Junggar. The confirmation of the Late Carboniferous back-arc basin basalts, together with other geological observations, indicate that an arc-basin evolutionary system still existed in southern West Junggar at *c.* 310 Ma, and the Junggar Ocean closed after Late Carboniferous time.

1. Introduction

The Central Asian Orogenic Belt (CAOB), located between the Siberian Craton to the north, European Craton to the west and Tarim–North China Craton to the south (Fig. 1a), is considered the largest Phanerozoic accretionary orogen in the world. It is characterized by a complicated tectonic evolution and significant crustal growth during Phanerozoic time (Jahn *et al.* 2000; Windley *et al.* 2007; Xiao *et al.* 2008; Windley & Xiao, 2018). As an important component of the southwestern segment of the CAOB, West Junggar in NW China is considered to be a critical area for Phanerozoic crustal growth owing to the occurrence of several early Palaeozoic ophiolitic mélange belts, voluminous Carboniferous volcanic–plutonic magmatism and a complex tectonic evolution (e.g. Jahn *et al.* 2004; Xiao *et al.* 2008; Geng *et al.* 2009; Zhang *et al.* 2011*a*; Choulet *et al.* 2012; Xiao & Santosh, 2014), and has long been of widespread concern in the geological community. However, the tectonic nature of the Late Carboniferous magmatism in southern West Junggar still remains controversial. Data for Late Carboniferous magmatic rocks showing diverse geochemical signatures and different ages (Fig. 1b) have led to very different interpretations of the Late Carboniferous tectonic setting of West Junggar.

Some researchers proposed that the West Junggar oceanic basin closed at ~320 Ma and was followed by the onset of post-collisional magmatism since Late Carboniferous time based on research on the detrital zircons in modern river sands and extensively distributed A-type granitoids (e.g. Han *et al.* 2006; Xu *et al.* 2012; Gao *et al.* 2014; Liu *et al.* 2019). However, many other scholars drew the conclusion that West Junggar was still in a subduction-dominated island arc setting during Late Carboniferous to Early Permian times according to the occurrence of voluminous calc-alkalic I-type granitoids, slab-derived adakites and sanukitic rocks in the region and systematic palaeogeographic and geological studies (e.g. Zhang *et al.* 2006; Xiao *et al.* 2008;
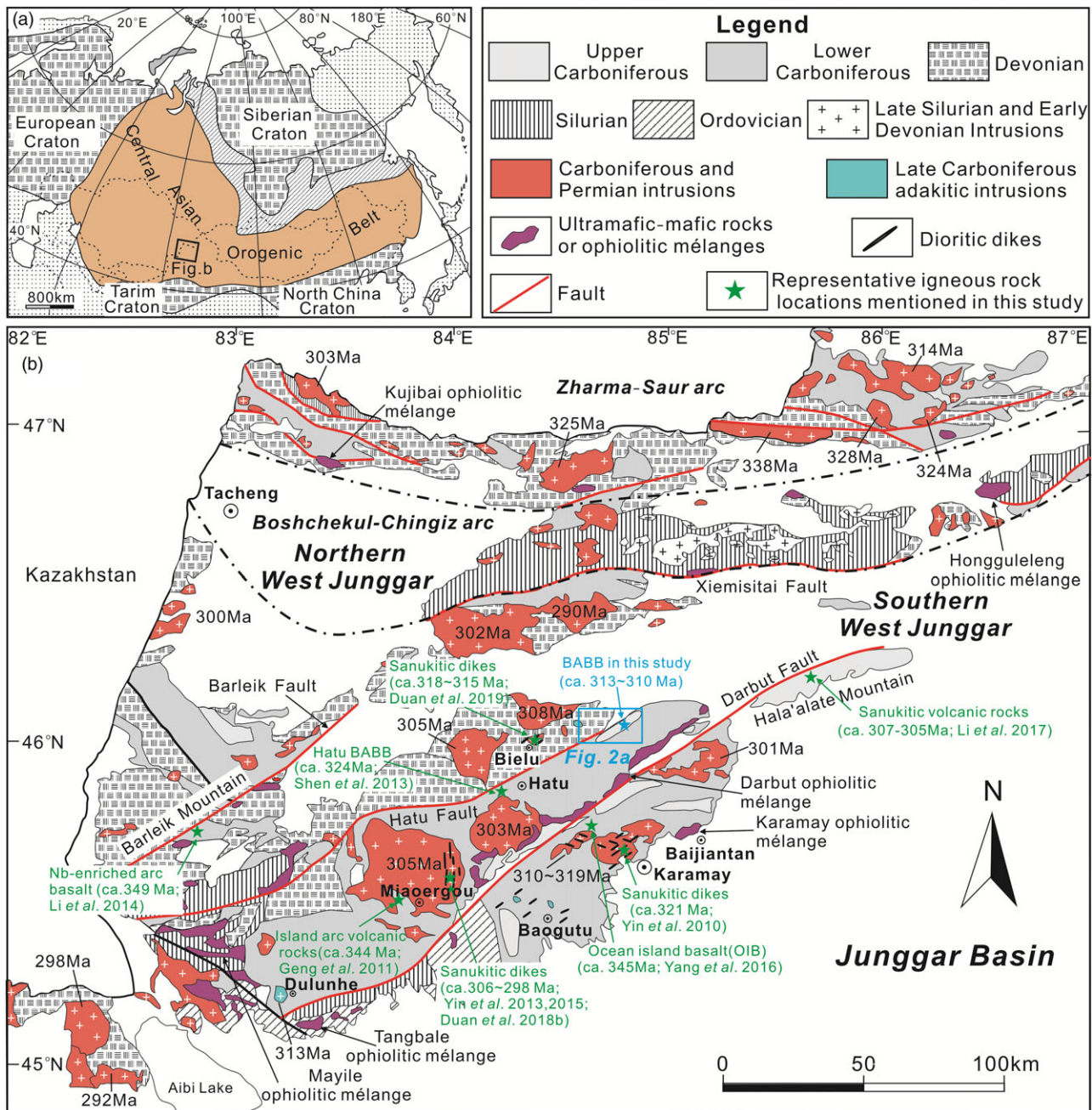
Fig. 1. (Colour online) (a) Simplified tectonic sketch of the Central Asian Orogenic Belt (after Jahn *et al.* 2000) and (b) regional geological map of southern West Junggar, Xinjiang (modified after BGMRXUAR, 1993; Duan *et al.* 2019).

Shen *et al.* 2009, 2012; Duan *et al.* 2015, 2018*a,b,c*, 2019; Li *et al.* 2017). Recently, a 321–290 Ma ridge subduction model based on the existence of some tholeiites, A-type granitoids, charnockites, adakites and high-Mg dioritic dykes in West Junggar has also been proposed (e.g. Geng *et al.* 2009; Tang *et al.* 2010, 2012; Yin *et al.* 2010, 2013, 2015; Windley & Xiao, 2018). Obviously, arguments remain concerning the Late Carboniferous tectonic regime of southern West Junggar despite numerous studies having been performed. Previous studies mainly concentrated on the granitoids (e.g. Chen & Arakawa, 2005; Han *et al.* 2006; Geng *et al.* 2009; Shen *et al.* 2009; Gao *et al.* 2014; Duan *et al.* 2015, 2018*a,b*), ophiolitic mélanges (Gu *et al.* 2009; Yang *et al.* 2012; Zhu *et al.* 2015 and related references therein) and dioritic dykes (e.g. Tang *et al.* 2010; Yin *et al.*

2010, 2013, 2015; Duan *et al.* 2018*c*, 2019) in the study area, with less attention paid to the volcanic rocks, especially to the Late Carboniferous volcanic rocks.

Basaltic magmas may be considered relatively reliable for constraining their tectonic settings. This is because basaltic magmas with distinctive geochemical characteristics are associated with specific tectonic settings. Recently, we identified a suite of Late Carboniferous back-arc basin basalts (BABB) from the Chengjisihanshan Formation in southern West Junggar. This study presents new laser-ablation inductively coupled plasma mass spectrometer (LA-ICP-MS) zircon U–Pb ages, major and trace elements, and Sr–Nd–Pb–Hf isotope data for the basaltic rocks. The data are used to shed light on the Late Carboniferous tectonic

setting of southern West Junggar, and also provide robust constraints on the tectonic evolution of the Junggar Ocean in Late Carboniferous time.

2. Geological background

2.a. Regional geology

West Junggar is composed of Palaeozoic intra-oceanic arcs and accretionary complexes and records accretionary processes in the southwestern part of the CAOB (Feng *et al.* 1989; Windley *et al.* 2007; Xiao *et al.* 2008; Choulet *et al.* 2012; Windley & Xiao, 2018; Zhang *et al.* 2018). It can generally be subdivided into northern and southern parts by the Xiemisitai Fault. Northern West Junggar is mainly composed of two nearly E–W-trending magmatic arcs; from north to south they are the late Palaeozoic Zharma-Saur and early–middle Palaeozoic Boshchekul-Chingiz magmatic arcs (Fig. 1b). Its Palaeozoic lithostratigraphy ranges in age from Ordovician to Permian (BGMRXUAR, 1993).

In contrast to the nearly E–W-trending faults in the northern part, southern West Junggar is characterized by several NE-trending faults, including the Barleik, Hatu and Darbut faults from west to east. Moreover, many ophiolitic mélanges are distributed along the major faults in the southern part (Fig. 1b), with their ages varying from late Neoproterozoic to latest Devonian, demonstrating a complicated accretionary history for the Palaeo-Asian Ocean. Additionally, late Palaeozoic intermediate to felsic granitic intrusions and dioritic dykes are also extensively distributed (Fig. 1b). Granitic intrusions mostly consist of A-type and I-type granitoids and adakites, and are characterized by their short emplacement duration (*c.* 329–287 Ma) and high positive $\varepsilon Nd(t)$ (+4.60 to +9.20) and $\varepsilon Hf(t)$ (+4.60 to +16.8) values with very young Nd and Hf model ages (e.g. Chen & Arakawa, 2005; Han *et al.* 2006; Geng *et al.* 2009; Shen *et al.* 2009; Tang *et al.* 2010, 2012; Gao *et al.* 2014; Duan *et al.* 2015, 2018*a,b*). The dioritic dykes intruded most of geologic bodies, with their ages clustering mainly around the Late Carboniferous to earliest Permian period (*c.* 321–292 Ma); some were reported with sanukitic high-Mg diorite features (Tang *et al.* 2010; Yin *et al.* 2010, 2013, 2015; Duan *et al.* 2018*c*, 2019).

The strata in the southern part are dominated by Devonian and Carboniferous volcaniclastic sediments, and are separated by the Hatu Fault, as shown in Figure 1b. The Devonian strata, distributed principally on the northwestern side of the Hatu Fault, consist mainly of neritic-littoral facies pyroclastic sediments and andesitic volcanic rocks. The Carboniferous volcano-sedimentary strata, including the Lower Carboniferous Heishantou, Baogutu and Xibeikulasi formations and Upper Carboniferous Chengjisihanshan Formation, are most widely distributed on both sides of the Darbut and Barleik faults. The Heishantou Formation, mainly distributed on Barleik Mountain, consists of volcaniclastic rocks, clastic rocks and Nb-enriched basalts and basaltic andesites (Li *et al.* 2014). The Baogutu Formation is composed of deep-sea facies fine-grained clastic rocks consisting of siliceous and muddy siltstone, tuffaceous siltstone, felsic tuff, variegated chert, limestone and basic to intermediate volcanic rocks with zircon U–Pb ages of *c.* 346–324 Ma (Guo *et al.* 2010; Geng *et al.* 2011; Shen *et al.* 2013; Yang *et al.* 2016). Previous studies have confirmed that the volcanic rocks within the Baogutu Formation distributed in the northern Karamay region possess alkaline oceanic island basalt characteristics (*c.* 346 Ma; Yang *et al.* 2016), and ~324 Ma tholeiites erupted in the Hatu region were reported to have BABB affinity (Shen *et al.* 2013). The Xibeikulasi Formation, conformably

overlying the Baogutu Formation on the southern side of the Hongshan pluton (Li *et al.* 2010), is characterized by conglomerate, pebbly sandstone and coarse sandstone, representing coarse debris flow deposits (BGMRXUAR, 1993; Li *et al.* 2010).

The studied basaltic rocks are hosted in the Upper Carboniferous Chengjisihanshan Formation. The Chengjisihanshan Formation, established by Xiang *et al* (2013), is characterized by basic to intermediate volcanic rocks consisting mainly of basalt, basaltic andesite and andesite, which are sandwiched within neritic facies of volcano-sedimentary rocks, including strongly cleaved pebbled sandstone, feldspathic lithic sandstone, thin-layered tuff, tuffaceous siltstone, fine sandstone and chert with minor limestone lenses. An angular unconformable contact between the Chengjisihanshan Formation and the Lower Carboniferous strata was observed at the stratotype section of the Chengjisihanshan Formation in the Baijiantan region, while fault contacts were observed in local areas (Xiang *et al.* 2013). Meanwhile, Moscovian fossils, such as *Choristites* sp. and *Pseudotimania* sp., were found in limestone lenses (Xiang *et al.* 2013), indicating that the Chengjisihanshan Formation was formed in Late Carboniferous time.

2.b. Geology and petrology of the Chengjisihanshan Formation

In the Suoerkuduke–Aletunzhawati area of southern West Junggar, we distinguished an assemblage of NE-trending volcanic rocks and their associated sedimentary rocks in the Chengjisihanshan Formation based on the results of a detailed geological survey at a scale of 1:5000 and sampling (Fig. 2a). The measured sections of A–A′ and B–B′ in the Aletunzhawati area preserve a suite of well-exposed volcanogenic–sedimentary rocks composed mainly of tuffaceous sandstone, feldspathic lithic sandstone, pebbled sandstone, conglomerate, chert, basalt and pyroxene basalt (Fig. 2b), presenting a clear red-coloured hue in the field (Fig. 3a, b, c). These volcanogenic–sedimentary rocks were strongly cleaved, while only a small number of interlaminar folds could be observed in the field. Volcanic rocks occurred as stratified or intercalated beds, and were in conformable contact with the chert and tuffaceous siltstone in section A–A′, or were in fault contact with the tuffaceous lithic sandstones in section B–B′ (Fig. 2b). Additionally, the occurrence of interbedded grey-green basalts and dark-red cherts (Fig. 3d) and basalt pillow structures (Fig. 3e) can be observed in some well-preserved outcrops.

Furthermore, a set of NE- to NEE- and subparallel W–E-striking faults were also developed in the study area. The NE- and NEE-striking faults cut through the eastern and southern boundaries of the Chengjisihanshan Formation, respectively, and separated this stratigraphic unit from the Lower Carboniferous Baogutu and Xibeikulasi formations (Fig. 2a). The strata of the Chengjisihanshan Formation in the study area dip steeply to the SE (Fig. 2b), and the vast majority of the sedimentary rocks are strongly cleaved owing to the influence of massive faults in the area during the later stage (Fig. 2a). Notably, a gabbro body with an outcrop area of *c.* 0.1 km² is observed in section B–B′ (Fig. 2b). The gabbro intruded into brecciated tuff and lithic sandstone, and showed a normal mid-oceanic ridge basalt (N-MORB) affinity with a zircon U–Pb age of 296.1 ± 2.7 Ma; it was believed to have originated from a depleted mantle source in an extensional tectonic setting (Zhang & Zhu, 2018).

In this contribution, basaltic samples were collected from the Chengjisihanshan Formation in the Aletunzhawati area. The basalt and pyroxene basalt are grey-green in hand specimen and are
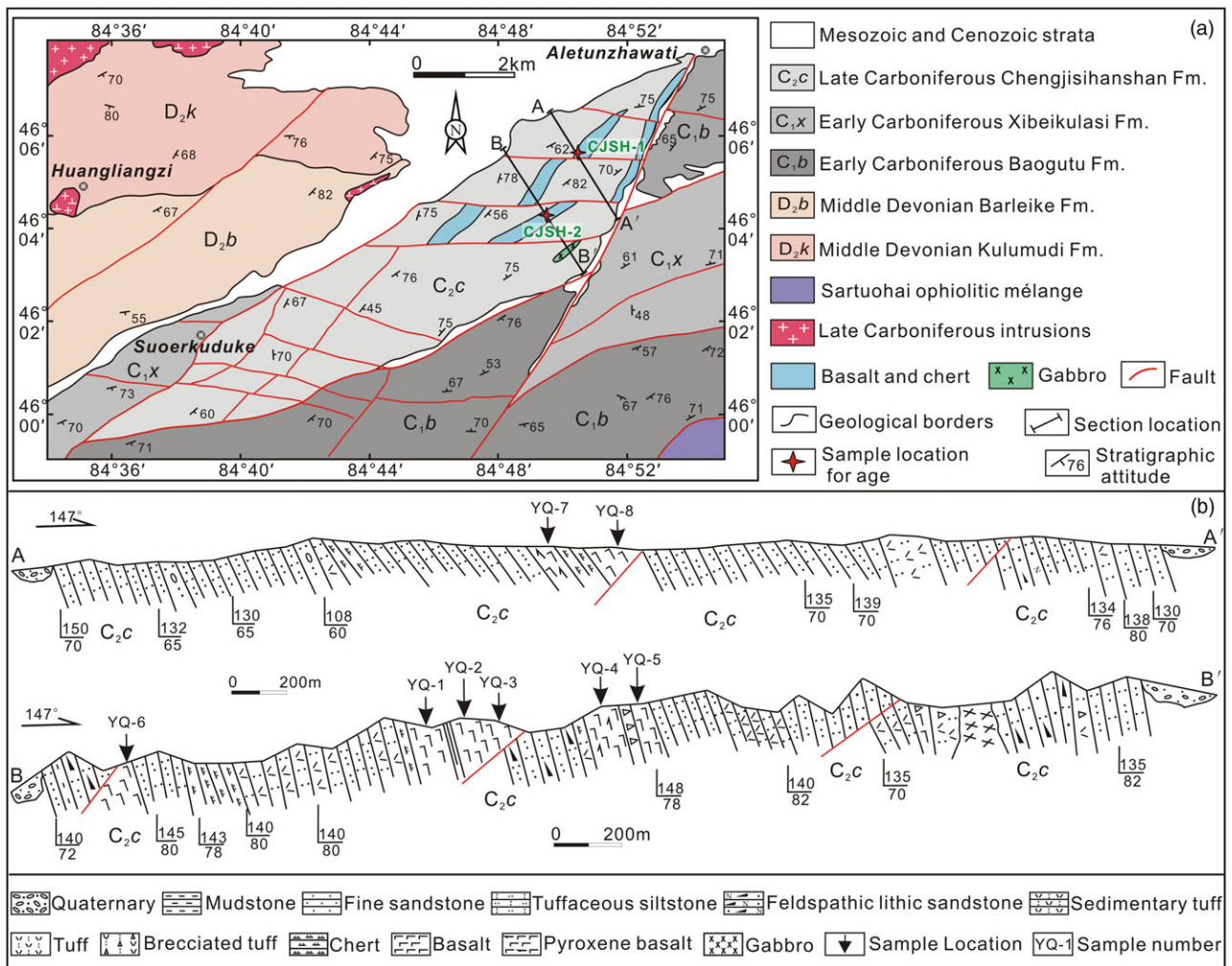
Fig. 2. (Colour online) (a) Geological map of the Aletunzhawati area. Lines A–A′ and B–B′ show the location of the measured sections. (b) Geological sections along A–A′ and B–B′ showing the volcanic rocks from the study area.

dominated by massive structures with porphyric textures. In thin-sections, the basaltic samples mainly contain pyroxene and plagioclase, and generally experienced varying degrees of epidotization and chloritization (Fig. 4). The basalt (Fig. 4a, b) and pyroxene basalt (Fig. 4c, d) have fine- to medium-grained or porphyritic textures, with ~10 % euhedral to subhedral phenocrysts of plagioclase and pyroxene up to 0.5 mm long in a groundmass (~90 %) of fine-grained to aphanitic plagioclase, pyroxene, chlorite, epidote and minor Fe–Ti oxides and opaque minerals.

3. Analytical methods

3.a. Zircon U–Pb dating

Zircon grains were separated by routine physical approaches employing elutriation, heavy liquids and magnetic techniques, and then carefully hand-picked under a binocular microscope, mounted in epoxy and polished down to their cores for analysis. In order to understand the internal structure of the zircon directly, cathodoluminescence (CL) images were taken using a Quanta 400FEG environmental scanning electron microscope at the State Key Laboratory of Continental Dynamics, Northwest University, China.

LA-ICP-MS zircon U–Pb dating was carried out at the Key Laboratory for the Study of Focused Magmatism and Giant Ore Deposits, MNR, Xi'an Centre of Geological Survey, CGS, China. Laser sampling was performed using a GeoLas Pro. An Agilent 7700x ICP-MS instrument was used to acquire ion-signal intensities. Helium was applied as a carrier gas. Argon was used as the make-up gas and mixed with the carrier gas via a T-connector before entering the ICP-MS. Each analysis incorporated a background acquisition of ~10 s (gas blank) followed by 40 s of data acquisition from the sample. The Agilent Chemstation was utilized for the acquisition of each individual analysis. Off-line selection and integration of background and analyte signals, and time-drift correction and quantitative calibration for trace-element analyses and U–Pb dating were performed using Glitter 4.4. Concordia diagrams and weighted mean calculations were made using Isoplot/Ex_ver 3 (Ludwig, 2003).

3.b. Whole-rock geochemical analyses

Whole-rock samples were ultrasonically cleaned repeatedly using diluted hydrochloric acid (3–5 wt %) to remove surface impurities, followed by coarse crushing to 2–4 cm. All of the samples were powdered to less than 200 mesh suitable for
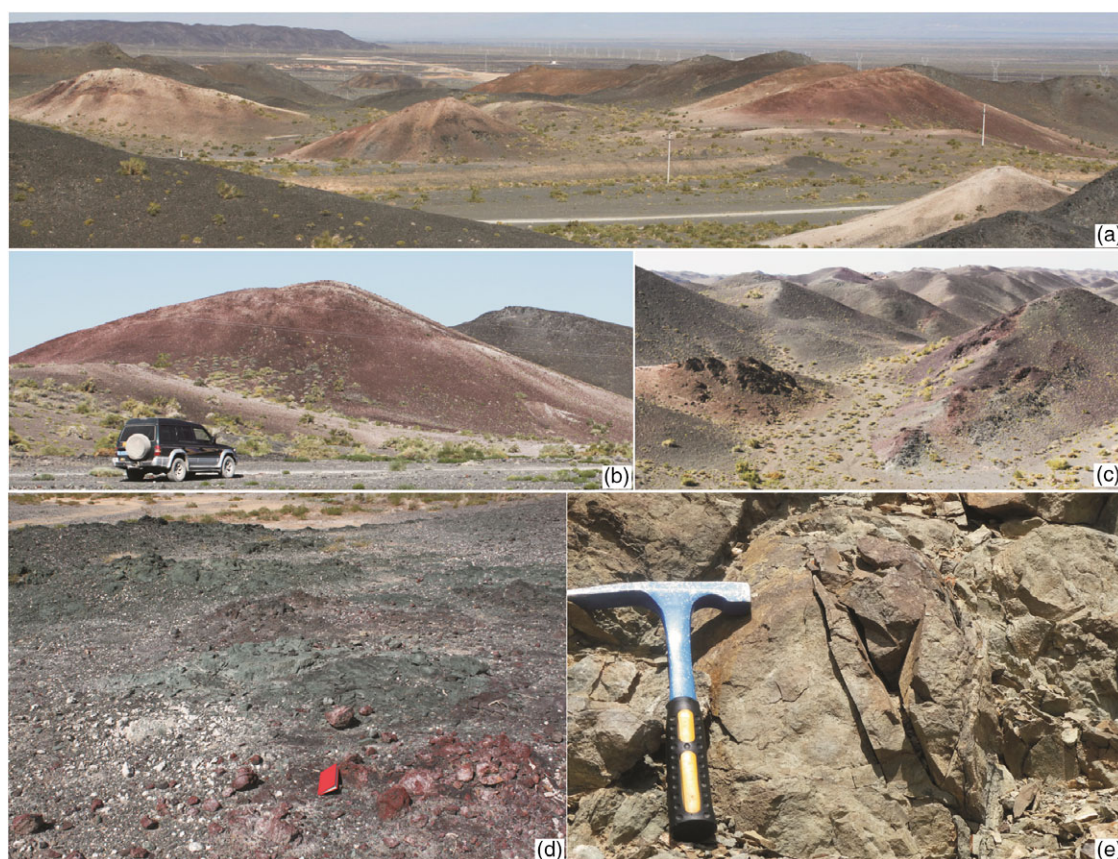
Fig. 3. (Colour online) Photos showing field outcrops of different components of the Chengjisihanshan Formation. (a–c) Field outcrops showing red-coloured hue; (d) occurrence of interbedded grey-green basalts and dark-red cherts; (e) pillow basalt. Hammer for scale is 285 mm long. Notebook for scale is 175 mm long.

analytical testing. Major- and trace-element analyses were conducted at the Ministry of Education Key Laboratory of Western China's Mineral Resources and Geological Engineering, Xi'an, China. The fused glass discs were made for major-element oxide testing by a condensation after the sufficiently homogeneous mixture of lithium borate flux with a 1:8 sample-to-$Li_2B_4O_7$–$LiBO_2$ flux ratio fused in an auto fluxer between 1050 °C and 1100 °C. Major-element contents were analysed using a Shimadzu LAB CENTER XRF-1800 sequential scanning X-ray fluorescence spectrometer, with analytical uncertainties of < 2 wt %. The loss on ignition (LOI) was weighed after baking for 90 min at a high temperature of 1000 °C in an oven. Trace and rare earth elements (REEs) were analysed using a Thermo-X7 ICP-MS. ICP-MS trace-element analyses were made after a standard acid-digestion procedure using a mixture of HF–HNO_3 and a sinter procedure using Na_2O_2 (for REEs). Standard reference materials SY-2 and MRG-1 were used to monitor the data quality during the course of this study. The precision and accuracy of the trace-element analyses are estimated to be better than 5 wt % (relative), except for Nb and Ta (better than 10 wt %).

3.c. Sr–Nd–Pb isotopic analyses

The whole-rock Sr–Nd isotopic ratios were determined using an IsoProbe-T thermal ionization mass spectrometer (TIMS) at the Analytical Laboratory, Beijing Research Institute of Uranium Geology, China. Sample powders were dissolved in a HF + HNO_3 + $HClO_4$ mixture. Digested samples were first dried and dissolved in 6N HCl, then dried again and redissolved in 0.5N

HCl for Sr and Nd separation or 0.5N HBr for Pb separation. Sr and Nd fractions were separated following standard chromatographic techniques using AG 50-X8 and PTFE-HDEHP resins with HCl as an eluent (Sato *et al.* 1995), while the Pb fraction was separated using a strong alkali anion exchange resin with HBr and HCl as eluents (Babinski *et al.* 1999; Marques *et al.* 1999). The mass fractionation corrections for Sr and Nd isotopic ratios are based on the $^{86}Sr/^{88}Sr$ ratio of 0.1194 and $^{146}Nd/^{144}Nd$ ratio of 0.7219, respectively. The $^{87}Sr/^{86}Sr$ ratio of the Standard NBS987 and $^{143}Nd/^{144}Nd$ ratio of the Standard SHINESTU determined in this study were 0.710250 ± 0.000007 (2σ) and 0.512118 ± 0.000003 (2σ), respectively. For whole-rock Pb isotopic determinations, ~100 mg of powder were weighed into a Teflon beaker, spiked and dissolved in concentrated HF at 180 °C for 7 h. Lead was separated and purified by a conventional cation-exchange technique (AG 1-X8, 20–400 resin). Total procedural blanks were < 50 pg Pb. Isotopic ratios were measured by a VG-354 mass spectrometer. Repeated analyses of SRM 981 yielded average values of $^{206}Pb/^{204}Pb = 16.9325 ± 3$ (2σ), $^{207}Pb/^{204}Pb = 15.4853 ± 3$ (2σ) and $^{208}Pb/^{204}Pb = 36.6780 ± 9$ (2σ). External precisions are less than 0.005, 0.005 and 0.0015.

3.d. In situ zircon Hf isotope analyses

In situ zircon Hf isotope analyses were performed using a GeoLas Pro laser-ablation system coupled to a Neptune multiple-collector ICP-MS at the Key Laboratory for the Study of Focused Magmatism and Giant Ore Deposits, MNR, Xi'an Centre of Geological Survey, CGS, China. A stationary GeoLas Pro
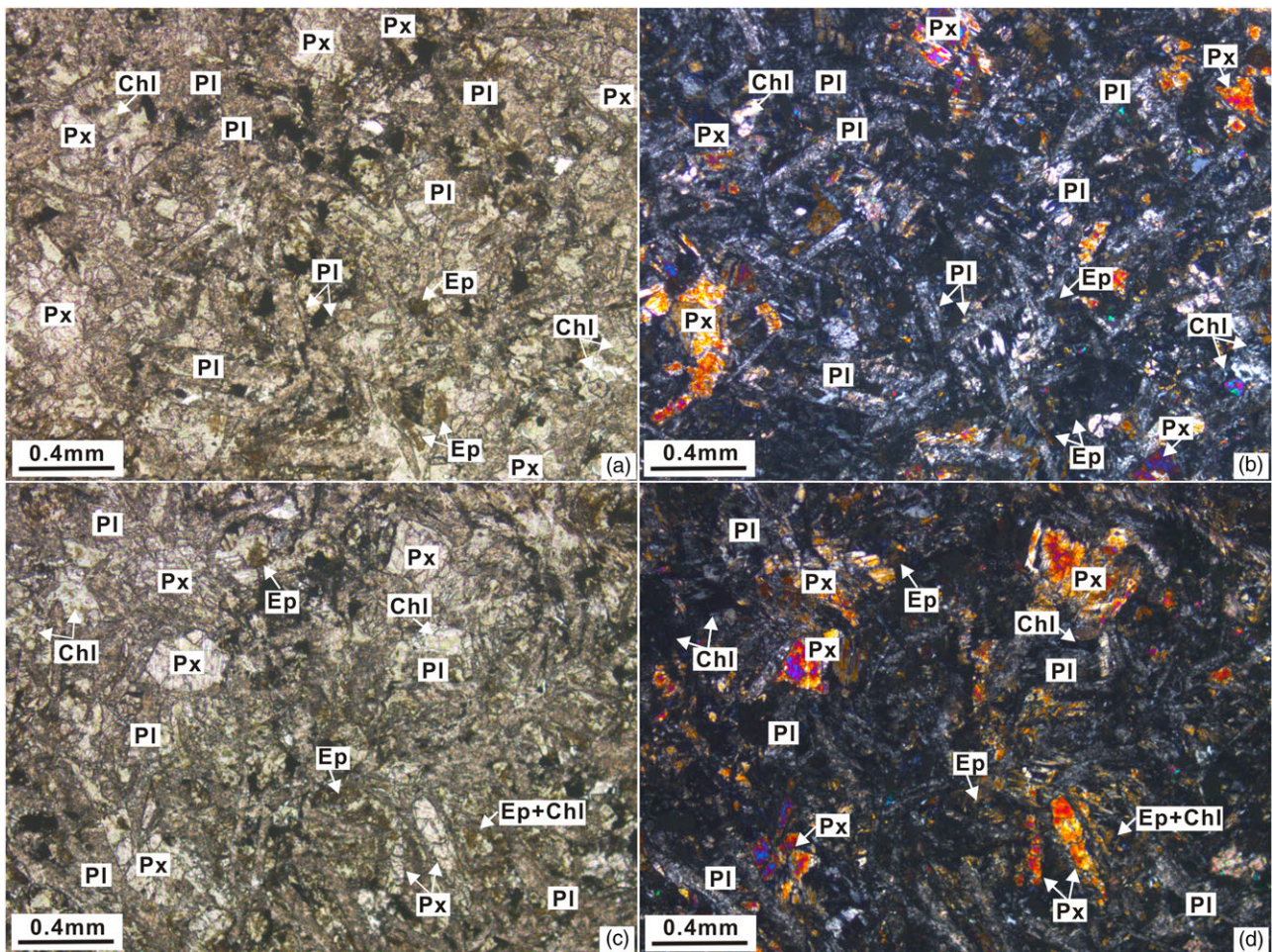
Fig. 4. (Colour online) Photomicrographs of (a, b) basalt and (c, d) pyroxene basalt in the Chengjisihanshan Formation viewed in polarized and cross-polarized light. Px – pyroxene; Pl – plagioclase; Chl – chlorite; Ep – epidote.

laser-ablation spot with a beam diameter of 32 µm was used for the analyses. All the Hf analyses were done on the same spot used for U–Pb laser ablation. The ablated material was transported from the laser-ablation cell using helium as a carrier gas, and then combined with argon in a mixing chamber before being introduced to the ICP-MS plasma. Correction for ^{176}Lu and ^{176}Yb isobaric interferences on ^{176}Hf used ^{176}Lu/^{175}Lu = 0.02658 and ^{176}Yb/^{173}Yb = 0.796218 (Chu *et al.* 2002), respectively. Zircon GJ-1 was used as the reference standard and yielded a weighted mean ^{176}Hf/^{177}Hf ratio of 0.282030 ± 40 (2σ) during this study. A decay constant for ^{176}Lu of 1.865 × 10^{-11}/a (Scherer *et al.* 2001) and the present-day chondritic ratios of ^{176}Hf/^{177}Hf = 0.282772 and ^{176}Lu/^{177}Hf = 0.0332 (Blichert-Toft & Albarède, 1997) were adopted to calculate εHf values. Single-stage model ages were calculated by reference to depleted mantle with a present-day ^{176}Hf/^{177}Hf ratio of 0.28325 and ^{176}Lu/^{177}Hf ratio of 0.0384 (Vervoot & Blichert-Toft, 1999).

4. Results

4.a. Zircon U–Pb geochronology

Two basaltic samples from the Chengjisihanshan Formation were chosen for LA-ICP-MS zircon U–Pb determination; their sampling locations are shown in Figure 2a, and the analytical results are listed in Table 1. Zircons separated from the basalt (CJSH-1) and pyroxene basalt (CJSH-2) are transparent, colourless or light yellow, and long prismatic in shape. The grains are 40–120 µm long and 30–90 µm wide with length–width ratios of 1:1 to 2.5:1. They have a well-developed but incomplete crystal morphology, and are half-baked with broad growth zoning or no growth zoning in CL images (Fig. 5), which is a typical feature of zircons from magmatic rocks with relatively low silica content (Corfu *et al.* 2003). Moreover, the chondrite-normalized REE distribution patterns of the zircons are consistent, characterized by light rare earth element (LREE) depletions, heavy rare earth element (HREE) enrichments, positive Ce anomalies and negative Eu anomalies (Fig. 6a), which are obviously different from those of hydrothermal zircons and consistent with typical magmatic-origin zircons (Zhao, 2010). Additionally, zircon grains from the two investigated basaltic samples have variable Th (23.3–465 ppm and 32.1–466 ppm, respectively) and U (48.3–887 ppm and 77.2–776 ppm, respectively) concentrations, and all zircons display relatively high Th/U ratios of 0.37–0.75 and 0.33–0.96, respectively (Table 1). They also exhibit favourable positive correlations between Th and U (Fig. 6b), further suggesting a magmatic origin (Belousova *et al.* 2002).

Twenty-nine zircon grains were analysed for basalt sample CJSH-1, and all the data are concordant or nearly concordant, yielding ^{206}Pb–^{238}U apparent ages of 304 Ma to 319 Ma

Table 1. LA-ICP-MS zircon U–Pb isotopic analysis of the basaltic rocks in the Chengjisihanshan Formation in southern West Junggar

Spot	Isotope concentrations (ppm)			Isotopic ratios						Age (Ma)					
	Th	U	Th/U	$^{207}Pb/^{206}Pb$	1σ	$^{207}Pb/^{235}U$	1σ	$^{206}Pb/^{238}U$	1σ	$^{207}Pb/^{206}Pb$	1σ	$^{207}Pb/^{235}U$	1σ	$^{206}Pb/^{238}U$	1σ
Basalt (CJSH-1)															
CJSH-1-01	392	726	0.54	0.05281	0.00157	0.36365	0.01056	0.05000	0.00105	321	32	315	8	315	6
CJSH-1-02	252	338	0.75	0.05372	0.00269	0.36957	0.01784	0.04995	0.00123	359	65	319	13	314	8
CJSH-1-03	80.4	168	0.48	0.05215	0.00199	0.35567	0.01320	0.04952	0.00110	292	46	309	10	312	7
CJSH-1-04	146	330	0.44	0.05338	0.00231	0.35632	0.01493	0.04846	0.00113	345	54	309	11	305	7
CJSH-1-05	65.2	150	0.43	0.05354	0.00186	0.36635	0.01237	0.04967	0.00108	352	39	317	9	312	7
CJSH-1-06	210	340	0.62	0.05325	0.00284	0.36485	0.01879	0.04974	0.00126	339	71	316	14	313	8
CJSH-1-07	79.8	186	0.43	0.05313	0.00221	0.37169	0.01499	0.05079	0.00117	334	51	321	11	319	7
CJSH-1-08	385	717	0.54	0.05286	0.00154	0.35522	0.01009	0.04878	0.00102	323	31	309	8	307	6
CJSH-1-09	179	398	0.45	0.05315	0.00156	0.36221	0.01039	0.04947	0.00104	335	31	314	8	311	6
CJSH-1-10	238	554	0.43	0.05380	0.00150	0.36690	0.00999	0.04950	0.00103	363	29	317	7	311	6
CJSH-1-11	153	281	0.55	0.05111	0.00211	0.35057	0.01403	0.04979	0.00112	246	52	305	11	313	7
CJSH-1-12	79.8	156	0.51	0.05306	0.00228	0.35464	0.01480	0.04851	0.00111	331	54	308	11	305	7
CJSH-1-13	53.1	144	0.37	0.05287	0.00381	0.36144	0.02518	0.04962	0.00141	323	107	313	19	312	9
CJSH-1-14	92.9	185	0.50	0.05341	0.00318	0.35498	0.02044	0.04824	0.00125	346	84	308	15	304	8
CJSH-1-15	207	340	0.61	0.05280	0.00161	0.36357	0.01077	0.04998	0.00106	320	33	315	8	314	7
CJSH-1-16	164	401	0.41	0.05373	0.00170	0.37348	0.01147	0.05045	0.00108	360	34	322	8	317	7
CJSH-1-17	174	412	0.42	0.05299	0.00175	0.35494	0.01134	0.04861	0.00105	328	36	308	8	306	6
CJSH-1-18	291	589	0.49	0.05365	0.00132	0.36478	0.00880	0.04934	0.00100	356	25	316	7	310	6
CJSH-1-19	23.3	48.3	0.48	0.05217	0.00395	0.35316	0.02587	0.04912	0.00140	293	115	307	19	309	9
CJSH-1-20	38.0	90.0	0.42	0.05202	0.00265	0.36414	0.01788	0.05079	0.00124	286	68	315	13	319	8
CJSH-1-21	235	581	0.40	0.05273	0.00138	0.35583	0.00909	0.04896	0.00100	317	27	309	7	308	6
CJSH-1-22	96.2	237	0.41	0.05269	0.00174	0.35479	0.01140	0.04886	0.00105	315	37	308	9	308	6
CJSH-1-23	314	699	0.45	0.05419	0.00175	0.37759	0.01182	0.05055	0.00108	379	35	325	9	318	7
CJSH-1-24	242	486	0.50	0.05253	0.00218	0.35548	0.01422	0.04909	0.00113	309	51	309	11	309	7
CJSH-1-25	79.6	196	0.41	0.05338	0.00196	0.35630	0.01265	0.04841	0.00107	345	42	309	9	305	7
CJSH-1-26	70.1	98.7	0.71	0.05104	0.00294	0.33989	0.01900	0.04830	0.00120	243	83	297	14	304	7
CJSH-1-27	198	274	0.72	0.05230	0.00300	0.35926	0.01991	0.04982	0.00128	299	80	312	15	313	8
CJSH-1-28	93.3	225	0.42	0.05190	0.00177	0.35061	0.01156	0.04899	0.00106	281	39	305	9	308	7
CJSH-1-29	465	887	0.52	0.05273	0.00120	0.35488	0.00791	0.04881	0.00098	317	23	308	6	307	6
Pyroxene basalt (CJSH-2)															
CJSH-2-01	226	249	0.91	0.06007	0.0035	0.40914	0.02321	0.04937	0.00143	606	121	348	17	311	9
CJSH-2-02	135	167	0.81	0.05165	0.00331	0.3687	0.0231	0.05175	0.0015	270	140	319	17	325	9
CJSH-2-03	403	440	0.92	0.05174	0.00313	0.35723	0.0211	0.05006	0.00145	274	133	310	16	315	9
CJSH-2-04	77.5	120	0.65	0.0546	0.0024	0.37588	0.01657	0.04992	0.00126	396	95	324	12	314	8
CJSH-2-05	181	265	0.68	0.05295	0.00353	0.37035	0.02406	0.05072	0.00153	327	144	320	18	319	9
CJSH-2-06	237	282	0.84	0.05335	0.00372	0.36766	0.02491	0.04998	0.00156	344	150	318	18	314	10
CJSH-2-07	351	702	0.50	0.05875	0.00229	0.42046	0.01641	0.05191	0.00133	558	83	356	12	326	8
CJSH-2-08	261	355	0.73	0.05001	0.00206	0.33732	0.01396	0.04892	0.00124	196	93	295	11	308	8
CJSH-2-09	327	390	0.84	0.06001	0.00312	0.41747	0.02129	0.05047	0.00142	604	109	354	15	317	9
CJSH-2-10	61.9	109	0.57	0.0562	0.00245	0.37047	0.01626	0.04782	0.00121	460	95	320	12	301	7

(Continued)

Table 1. (*Continued*)

Spot	Isotope concentrations (ppm)			Isotopic ratios							Age (Ma)				
	Th	U	Th/U	$^{207}Pb/^{206}Pb$	1σ	$^{207}Pb/^{235}U$	1σ	$^{206}Pb/^{238}U$	1σ	$^{207}Pb/^{206}Pb$	1σ	$^{207}Pb/^{235}U$	1σ	$^{206}Pb/^{238}U$	1σ
CJSH-2-11	50.8	77.2	0.66	0.05283	0.00406	0.36229	0.02732	0.04975	0.00153	322	165	314	20	313	9
CJSH-2-12	466	776	0.60	0.05373	0.00198	0.37416	0.01403	0.05052	0.00128	360	81	323	10	318	8
CJSH-2-13	152	282	0.54	0.05243	0.00181	0.35153	0.0125	0.04864	0.0012	304	77	306	9	306	7
CJSH-2-14	262	272	0.96	0.05465	0.00183	0.36874	0.01279	0.04895	0.00121	398	73	319	9	308	7
CJSH-2-15	32.1	97.5	0.33	0.05226	0.00292	0.35088	0.01952	0.04871	0.00132	297	122	305	15	307	8
CJSH-2-16	323	416	0.78	0.05634	0.00245	0.38252	0.01666	0.04926	0.00131	465	94	329	12	310	8
CJSH-2-17	148	254	0.58	0.05269	0.00169	0.3594	0.0121	0.0495	0.00122	316	71	312	9	311	7
CJSH-2-18	57.0	116	0.49	0.05345	0.00367	0.37216	0.02512	0.05053	0.00153	348	148	321	19	318	9
CJSH-2-19	170	202	0.84	0.06081	0.00286	0.43196	0.0203	0.05155	0.00142	632	98	365	14	324	9
CJSH-2-20	77	126	0.61	0.05287	0.00354	0.36175	0.02386	0.04965	0.0015	323	145	314	18	312	9

(Table 1), with a weighted mean age of 310.3 ± 3.9 Ma (MSWD = 0.16, *n* = 29) (Fig. 7a). Twenty zircon grains were analysed for pyroxene basalt sample CJSH-2, and the data are also concordant, yielding ^{206}Pb–^{238}U ages of 301 Ma to 326 Ma (Table 1), with a weighted mean age of 313.0 ± 5.7 Ma (MSWD = 0.27, *n* = 20) (Fig. 7b). All tested zircon grains lack visible inherited cores, and, thus, we consider the *c.* 313–310 Ma age to be the crystallization age of the basaltic rocks in the Chengjisihanshan Formation, which is consistent with the Moscovian fossil ages reported by Xiang *et al.* (2013).

4.b. Major-element contents

Major-element data for eight samples in this study are listed in Table 2, and their sampling locations are shown in Figure 2b. The investigated basalts and pyroxene basalts from the Chengjisihanshan Formation display minor variations in SiO_2 and Al_2O_3 ranging from 47.76 to 52.06 wt % and from 13.26 to 14.39 wt %, respectively. The contents of MgO are 6.55–7.68 wt %, with Mg no. (100 × molar Mg/(Mg + ΣFe)) values varying from 52.9 to 58.9. These rocks have relatively high TiO_2 (1.09–1.36 wt %) and TFe_2O_3 (11.22–13.58 wt %) contents but low K_2O (0.05–0.74 wt %) and P_2O_5 (0.06–0.09 wt %) contents (Table 2), and plot in the sub-alkaline basalt field on the Nb/Y–Zr/TiO_2 diagram (Fig. 8a; Winchester & Floyd, 1977) and define a typical tholeiite compositional trend on the SiO_2–FeO^T/MgO diagram (Fig. 8b; Miyashiro, 1974).

4.c. Trace-element compositions

The studied tholeiitic rocks are low in REE concentrations (ΣREE = 37.8–49.8 ppm) and display nearly flat REE patterns ((La/Yb)$_N$ = 0.87–1.07) with no to slightly positive Eu anomalies (Eu/Eu* = 0.99–1.16, only one sample 1.48) on the chondrite-normalized REE diagram (Fig. 9a), suggesting an N-MORB affinity. These rocks also have ratios of Lu/Yb (~0.15), Zr/Y (~2.53) and Y/Tb (~34) similar to those of N-MORB (Sun & McDonough, 1989), but are relatively enriched in LREEs and large ion lithophile elements (LILEs) such as U, and depleted in Nb, Ta, Ti, Zr and Hf compared to the neighbouring incompatible elements on the

N-MORB-normalized trace-element spidergrams (Fig. 9b), sharing an island arc basalt affinity (e.g. Perfit *et al.* 1980).

4.d. Sr–Nd–Pb–Hf isotope compositions

Two basaltic samples from the Chengjisihanshan Formation were chosen for Sr–Nd–Pb isotope analyses. Measured and initial isotopic ratios (back-calculated to 310 Ma) are reported in Table 3. All of the samples show a limited range in their $^{143}Nd/^{144}Nd$ and $^{87}Sr/^{86}Sr$ ratios. Initial $^{87}Sr/^{86}Sr$ ratios of the basaltic rocks are 0.70571 and 0.70573. Their initial Nd isotopes display small variations of 0.51245 and 0.51246 and calculated εNd(t) values of +4.21 and +4.36 (Table 3). The measured $^{206}Pb/^{204}Pb$, $^{207}Pb/^{204}Pb$ and $^{208}Pb/^{204}Pb$ ratios are 18.415 and 18.537, 15.536 and 15.552, 38.367 and 38.770, respectively, and their corresponding initial Pb isotopic ratios are less variable with ($^{206}Pb/^{204}Pb_i$) = 17.775–17.812, ($^{207}Pb/^{204}Pb_i$) = 15.504–15.512 and ($^{208}Pb/^{204}Pb_i$) = 37.687–37.781 (Table 3).

Two samples of zircons dated by U–Pb methods were also analysed for their in situ Lu–Hf isotope compositions, and the results are presented in Table 4. Seven zircon spot analyses were obtained for the basalt sample CJSH-1 (*c.* 310 Ma), yielding variable εHf(t) values in the range between +13.2 and +15.7 and initial $^{176}Hf/^{177}Hf$ ratios between 0.282959 and 0.283027 with juvenile two-stage model ages (T_{DM2}) mainly from 321 to 481 Ma. Similarly, six spot analyses were also made for the pyroxene basalt sample CJSH-2 (*c.* 313 Ma). The determined positive εHf(t) values for this sample vary between +8.06 and +14.9, and their initial $^{176}Hf/^{177}Hf$ ratios vary between 0.282811 and 0.283013, corresponding to T_{DM2} model ages in the range of 373 to 810 Ma.

5. Discussion

5.a. Crustal contamination and fractional crystallization

The basaltic samples exhibit negative Nb–Ta anomalies on the N-MORB-normalized trace-element spidergrams (Fig. 9b). The Nb–Ta troughs are typical characteristics of arc-related magma, but rocks formed by the contamination of crustal materials can also develop this anomaly (e.g. Pearce & Peate, 1995). However, their high Mg no. values (52.9–58.9), low La/Nb (1.51–1.67 < 12),
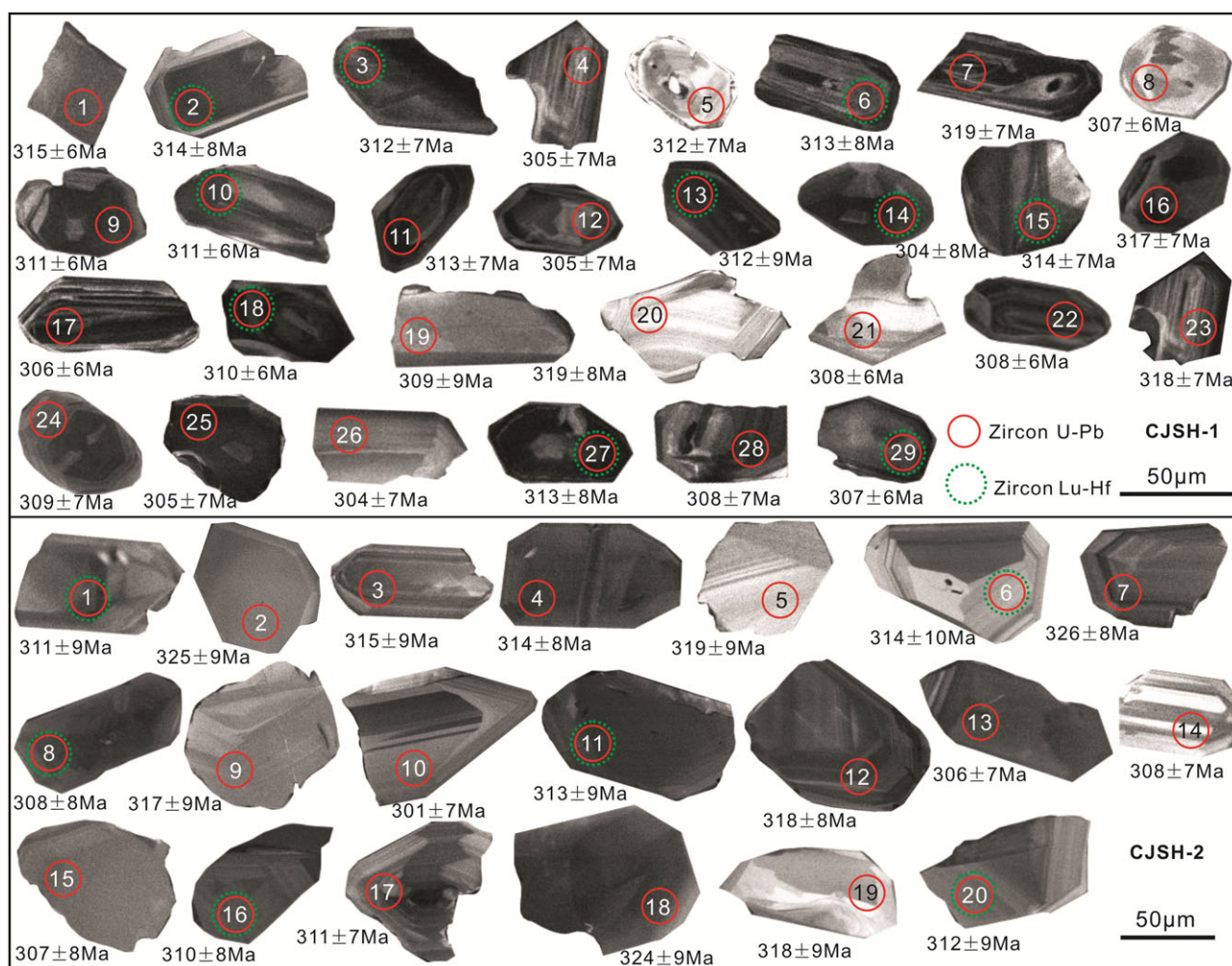
Fig. 5. (Colour online) Representative CL images and U–Pb apparent ages of zircons from the basaltic rocks in the Chengjisihanshan Formation.

Th/Ce (~0.06 < 0.15) and Th/La (0.06–0.07 < 0.3) ratios, together with the absence of inherited zircons (Fig. 5), indicate that crustal contamination did not play a significant role in the generation of the magmas (Lassiter & DePaolo, 1997; Plank, 2005). Moreover, the presence of basaltic samples with higher contents of Na_2O than K_2O (Table 2) also supports this view, which is incompatible with remarkable involvement of crustal materials. More importantly, the samples have high positive εHf(t) and εNd(t) values, which are typical features of the depleted mantle, and further preclude the possibility of significant crustal contamination. We therefore consider that the trace-element characteristics most likely reflect the mantle source signature and magmatic process during the magmas' ascent.

The basaltic rocks show relatively low CaO/Al_2O_3 ratios of 0.22–0.69, which, together with the positive correlation between the CaO/Al_2O_3 ratios and MgO contents suggest the possibility of clinopyroxene fractionation (Fig. 10a; Naumann & Geist, 1999). However, the consistent Mg no. (52.9–58.9) values and Cr (175–209 ppm) and Ni (88.3–104 ppm) concentrations and the lack of correlation between Cr, Ni and MgO are indicative of insignificant olivine fractionation (Fig. 10b, c). In addition, the basaltic rocks show no to slightly positive Eu anomalies (Eu/Eu* = 0.99–1.48) on the chondrite-normalized REE diagram (Fig. 9a), demonstrating negligible plagioclase fractionation.

Moreover, the negative correlation between TiO_2 and MgO indicates that Fe–Ti oxide fractionation did not play any major role in the magma evolution (Fig. 10d).

5.b. Origins of the basaltic rocks

Petrographically, the basaltic rocks from the Chengjisihanshan Formation underwent varying degrees of low-temperature hydrothermal alteration, as verified by the occurrence of secondary minerals such as epidote and chlorite (Fig. 4) and relatively high LOI values of 2.33 to 5.10 wt % (Table 2). Therefore, the immobile high field strength elements (e.g. Ti, Zr, Y, Nb and REEs) will be used in the following discussion to characterize the origin and possible tectonic environment of the basaltic rocks.

The tholeiitic rocks from the Chengjisihanshan Formation display low SiO_2 (47.76–52.06 wt %) but high MgO (6.55–7.68 wt %) contents and Mg no. (52.9–58.9) values with relatively high Sc, Co and Ni (43.1–52.3 ppm, 46.2–54.1 ppm and 88.3–104 ppm, respectively) concentrations, and also show subparallel REE patterns comparable to those of N-MORB (Fig. 9), indicative of a similar mantle source (Rapp & Watson, 1995). However, the studied basaltic rocks are characterized by high field strength element depletions relative to LILEs with negative Nb, Ta, Ti, Zr and Hf anomalies in the N-MORB-normalized multi-element plots
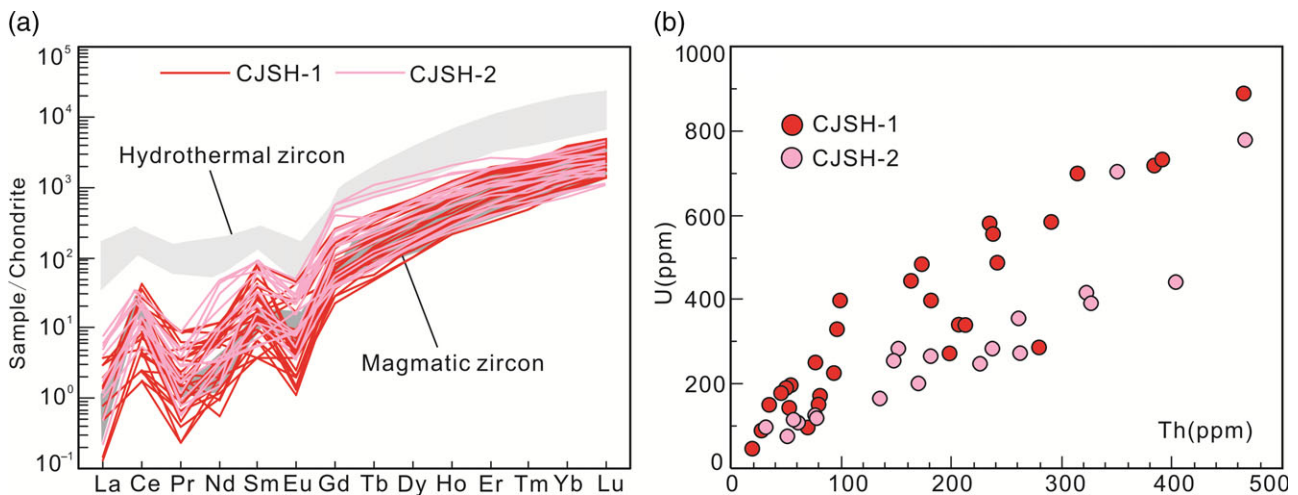
Fig. 6. (Colour online) (a) Chondrite-normalized rare earth element patterns and (b) Th–U diagram for zircons from the basaltic rocks in the Chengjisihanshan Formation (chondrite-normalized values are from Sun & McDonough, 1989; shaded areas after Zhao, 2010).
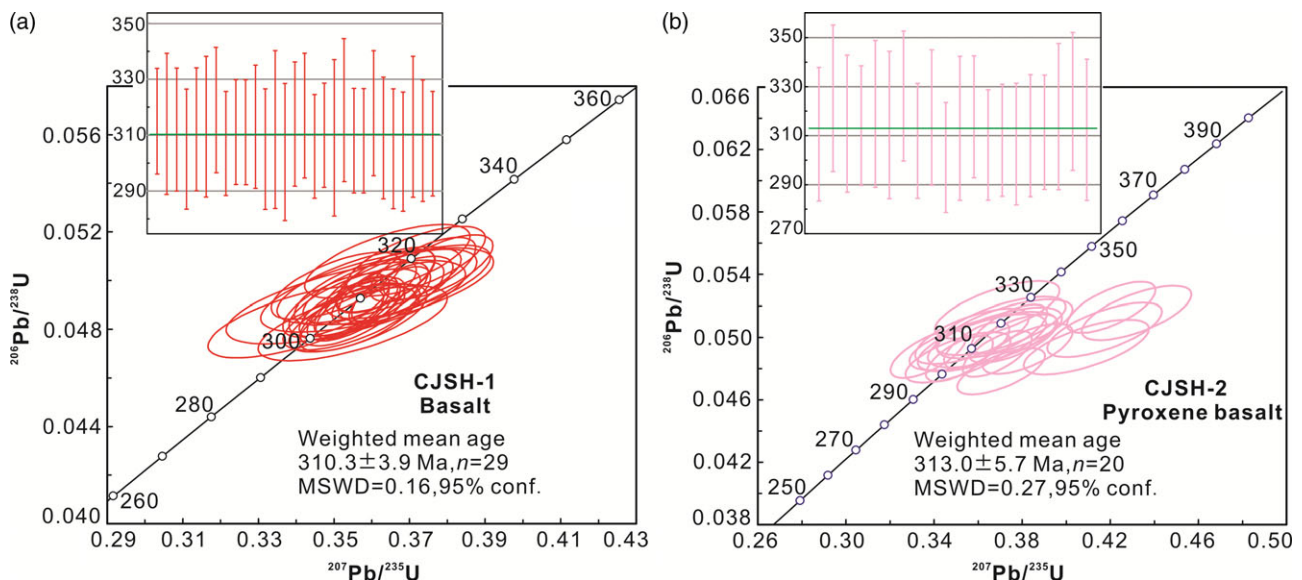
Fig. 7. (Colour online) LA-ICP-MS zircon U–Pb concordia diagrams for the basaltic rocks in the Chengjisihanshan Formation.

(Fig. 9b) in comparison with the N-MORB-derived magma, which is a typical feature of volcanic arc basalts (e.g. Perfit *et al.* 1980), reflecting the addition of slab-derived components in a subduction zone (Pearce & Peate, 1995; Pearce *et al.* 2005; Hémond *et al.* 2006). Moreover, they have low total REE concentrations (37.8–49.8 ppm) with their Nb/La (0.74–0.87) and Nb/Ta (12.0–13.0) ratios being lower than those of N-MORB (0.93 and 17.7, respectively; Sun & McDonough, 1989), further suggesting that additional slab-derived components were added into their mantle source, and these samples have experienced a subduction-related enrichment process (Pearce & Peate, 1995).

Subduction-related components generally comprise slab-derived fluids or melts, and the input of such components would produce different geochemical signatures in the magma. Partial melting of mantle metasomatized by slab-derived fluids would produce magmas with high Ba/Th ratios, while partial melting of mantle metasomatized by slab-derived melts may yield high

Th/Ta ratios (Pearce *et al.* 2005). The high Ba/Th (164–1612, with the exception of only one sample) and low Th/Ta ratios (1.24–1.48) of the studied rocks imply the influence of slab-derived fluids. In addition, their large compositional variations of Rb/Y (0.05–0.63) and Sr/Nd (41.5–153) but low and constant Nb/Y (0.12–0.14) and Th/Yb (0.10–0.13) ratios also strongly suggest that the subduction components were most likely dominated by slab-derived fluids (Hawkesworth *et al.* 1997; Woodhead *et al.* 2001). It was also confirmed that the Nb/U and Ce/Pb ratios of magma derived from the mantle will significantly decrease with the addition of slab fluids (Klein & Karsten, 1995). The results show that the Nb/U (19.4–37.5; 29.1 on average) and Ce/Pb (11.0–31.6; 22.9 on average) ratios of the basaltic rocks are remarkably lower than those of depleted mantle (47 ± 10 and 25 ± 5, respectively; Hofmann *et al.* 1986), further indicating the involvement of slab fluids in the magma-generation process (Klein & Karsten, 1995). More insights into the amount of involvement of slab fluids come from

Table 2. Geochemical compositions of the basaltic rocks from the Chengjisihanshan Formation

Sample	YQ-1	YQ-2	YQ-3	YQ-5	YQ-6	YQ-8	YQ-4	YQ-7
Lithology	basalt						pyroxene basalt	
Major elements (wt %)								
SiO_2	48.83	51.33	50.70	50.94	52.06	47.76	49.68	50.33
TiO_2	1.36	1.30	1.21	1.16	1.22	1.09	1.21	1.22
Al_2O_3	14.39	14.37	14.03	13.35	13.88	13.26	14.05	14.23
TFe_2O_3	13.32	13.58	11.72	11.22	13.10	12.52	12.99	12.32
MnO	0.20	0.12	0.19	0.16	0.13	0.17	0.19	0.17
MgO	7.56	6.55	7.04	6.91	6.90	7.68	7.52	7.19
CaO	6.68	4.48	7.60	8.71	3.03	9.20	9.62	7.01
Na_2O	2.34	3.11	3.45	3.59	4.00	3.35	1.32	3.69
K_2O	0.32	0.38	0.74	0.13	0.05	0.46	0.33	0.61
P_2O_5	0.08	0.09	0.08	0.08	0.06	0.07	0.08	0.07
LOI	4.86	4.36	3.11	2.33	5.10	2.57	3.64	3.52
Total	99.94	99.67	99.87	98.58	99.53	98.13	100.6	100.4
Mg no.	57.0	52.9	58.3	58.9	55.1	58.8	57.4	57.6
Trace elements (ppm)								
Sc	50.8	52.0	52.3	49.7	43.1	46.9	50.4	46.1
Cr	178	202	195	176	199	209	175	208
Co	54.0	54.1	53.8	46.2	50.7	47.6	48.9	49.4
Ni	99.9	104	103	88.3	96.6	93.9	90.4	90.8
Rb	8.43	7.64	14.0	2.46	1.04	6.31	6.34	7.27
Sr	189	132	369	159	253	132	190	412
Y	26.3	25.4	22.4	20.9	21.0	20.3	23.8	20.3
Zr	61.8	61.7	59.9	53.6	53.7	51.7	58.2	54.2
Nb	3.20	3.18	3.01	2.86	2.68	2.59	2.95	2.70
Cs	0.75	0.32	1.89	0.13	0.28	0.26	0.18	0.30
Ba	55.9	354	548	55.9	2582	113	112	380
La	5.19	5.30	4.80	4.56	4.38	4.13	4.75	4.09
Ce	11.3	11.8	10.3	9.50	9.01	8.46	10.3	8.44
Pr	1.74	1.81	1.62	1.44	1.44	1.32	1.61	1.32
Nd	9.27	9.56	8.49	7.67	7.41	7.05	8.38	7.09
Sm	3.19	3.06	2.69	2.60	2.59	2.38	2.90	2.41
Eu	1.17	1.27	1.22	0.97	1.65	1.01	1.14	1.05
Gd	4.08	4.26	3.88	3.42	4.40	3.18	3.72	3.33
Tb	0.77	0.77	0.67	0.63	0.63	0.62	0.69	0.61
Dy	5.05	5.03	4.42	4.15	4.24	4.00	4.67	4.04
Ho	1.07	1.07	0.95	0.86	0.88	0.85	0.99	0.86
Er	3.21	3.15	2.72	2.54	2.64	2.58	3.00	2.55
Tm	0.47	0.43	0.41	0.38	0.37	0.39	0.42	0.37
Yb	2.95	2.89	2.63	2.43	2.43	2.51	2.81	2.56
Lu	0.43	0.41	0.42	0.38	0.33	0.38	0.43	0.37
Hf	2.05	1.97	1.90	1.72	1.74	1.64	1.84	1.71
Ta	0.25	0.25	0.25	0.22	0.21	0.21	0.23	0.21

(*Continued*)

Table 2. (*Continued*)

Sample	YQ-1	YQ-2	YQ-3	YQ-5	YQ-6	YQ-8	YQ-4	YQ-7
Lithology	basalt						pyroxene basalt	
Pb	0.52	0.37	0.43	0.35	0.33	0.77	0.49	0.44
Th	0.34	0.35	0.34	0.31	0.27	0.26	0.34	0.27
U	0.13	0.16	0.09	0.08	0.13	0.08	0.10	0.08
ΣREE	48.9	49.8	44.2	40.5	41.4	37.8	44.8	38.0
Eu/Eu*	0.99	1.08	1.16	0.99	1.48	1.13	1.06	1.14
$(La/Yb)_N$	1.02	1.07	1.04	1.05	1.00	0.90	0.96	0.87
$(La/Sm)_N$	0.85	0.91	0.91	0.88	0.84	0.85	0.83	0.83
$(Gd/Yb)_N$	1.14	1.22	1.22	1.17	1.50	1.05	1.10	1.08

Note: LOI – loss on ignition; Mg no. = (100 × molar Mg/(Mg + ΣFe)); Eu/Eu* = $Eu_N/(Sm_N \times Gd_N)^{1/2}$; normalization values from Sun & McDonough (1989).
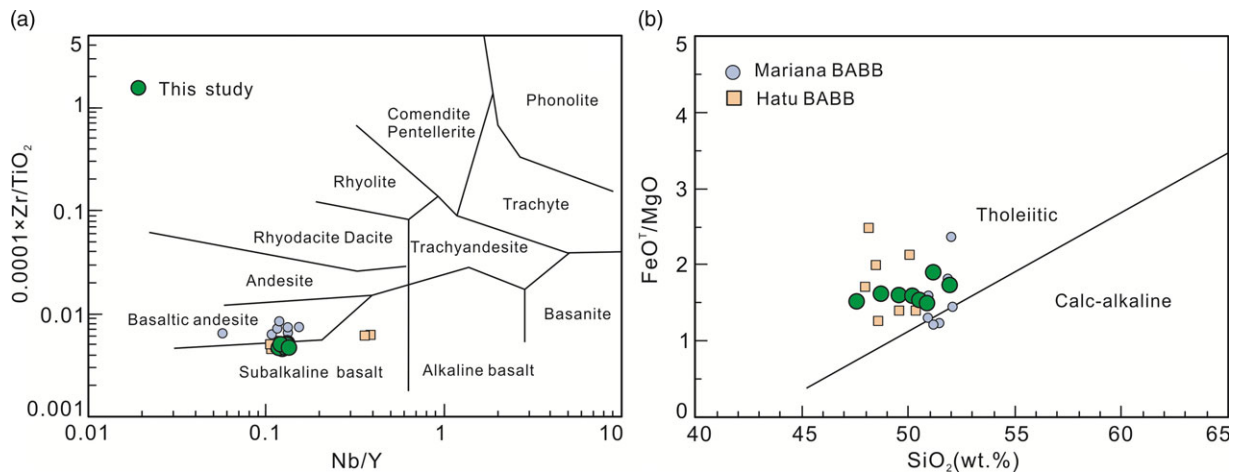
Fig. 8. (Colour online) (a) 0.0001 × Zr/TiO_2–Nb/Y (Winchester & Floyd, 1977) and (b) FeO^T/MgO–SiO_2 (Miyashiro, 1974) diagrams for the basaltic rocks. Data from Mariana BABB (Pearce *et al.* 2005) and Hatu BABB (Shen *et al.* 2013) are shown for comparison.
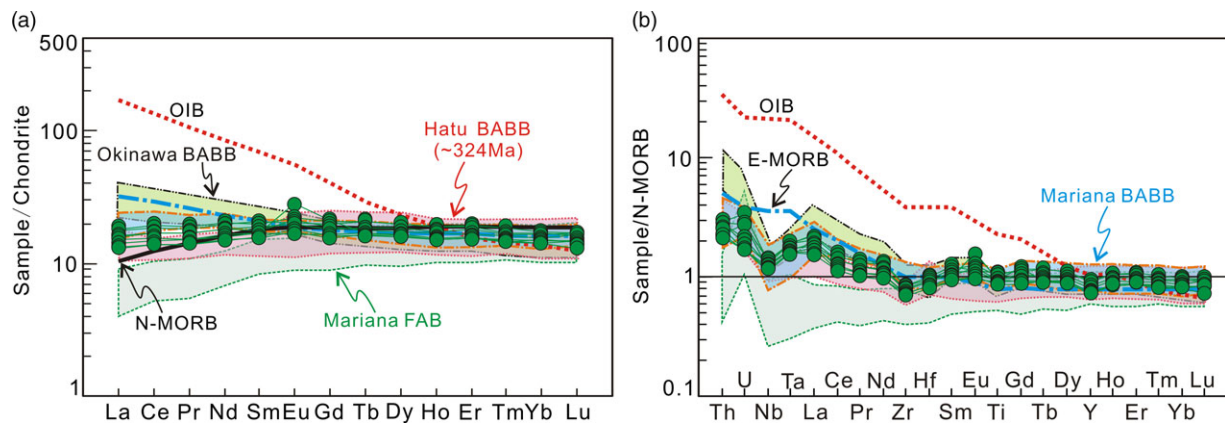
Fig. 9. (Colour online) (a) Chondrite-normalized rare earth element and (b) N-MORB-normalized trace-element patterns for the basaltic rocks. Chondrite, normal mid-ocean ridge basalt (N-MORB), enriched mid-ocean ridge basalt (E-MORB) and ocean island basalt (OIB) compositions are from Sun & McDonough (1989). Data for the Mariana FAB are from Reagan *et al.* (2010) and for the Okinawa, Mariana and Hatu BABBs are from Shinjo *et al.* (1999), Pearce *et al.* (2005) and Shen *et al.* (2013), respectively.

Table 3. Whole-rock Sr–Nd–Pb isotopic compositions of the basaltic rocks in the Chengjisihanshan Formation

Sample	Rb (ppm)	Sr (ppm)	$^{87}Rb/^{86}Sr$	$^{87}Sr/^{86}Sr$	$\pm2\sigma$	$(^{87}Sr/^{86}Sr)_i$	Sm (ppm)	Nd (ppm)	$^{147}Sm/^{144}Nd$	$^{143}Nd/^{144}Nd$
YQ-5	2.46	159	0.0447	0.70591	0.000015	0.70571	2.60	7.67	0.2063	0.51287
YQ-7	7.27	412	0.0511	0.70595	0.000018	0.70573	2.41	7.09	0.2069	0.51288

Sample	$\pm 2\sigma$	$(^{143}Nd/^{144}Nd)_i$	$\varepsilon_{Nd}(t)$	Pb (ppm)	$^{206}Pb/^{204}Pb$	$^{207}Pb/^{204}Pb$	$^{208}Pb/^{204}Pb$	$(^{206}Pb/^{204}Pb)_i$	$(^{207}Pb/^{204}Pb)_i$	$(^{208}Pb/^{204}Pb)_i$
YQ-5	0.000007	0.51245	4.21	0.35	18.537	15.552	38.770	17.77	15.51	37.78
YQ-7	0.000007	0.51246	4.36	0.44	18.415	15.536	38.367	17.81	15.50	37.69

Note: $^{87}Rb/^{86}Sr$ and $^{147}Sm/^{144}Nd$ ratios are calculated using Rb, Sr, Sm and Nd concentrations; decay constants used are 1.42×10^{-11}/a for ^{87}Rb (Steiger & Jäger, 1977) and 6.54×10^{-12}/a for ^{147}Sm (Lugmair & Marti, 1978); $\varepsilon Nd(t)$ values are calculated using present-day $(^{147}Sm/^{144}Nd)_{CHUR} = 0.1967$ and $(^{143}Nd/^{144}Nd)_{CHUR} = 0.512638$ (Wasserburg *et al.* 1981); $\lambda^{238}U = 1.55125 \times 10^{-10}$/y, $\lambda^{235}U = 9.8485 \times 10^{-10}$/y, $\lambda^{232}Th = 4.9475 \times 10^{-11}$/y (Steiger & Jäger, 1977).

Table 4. Zircon Hf isotopic compositions of the basaltic rocks in the Chengjisihanshan Formation

| Sample	$^{176}Lu/^{177}Hf$	$^{176}Yb/^{177}Hf$	$^{176}Hf/^{177}Hf$	2σ	$\varepsilon_{Hf}(0)$	$\varepsilon_{Hf}(t)$	2σ	t	T_{DM1} (Ma)	T_{DM2} (Ma)	$f_{Lu/Hf}$
Basalt (CJSH-1)											
2	0.001195	0.026377	0.282996	0.000023	7.9	14.5	0.83	310	365	397	−0.96
6	0.000724	0.017126	0.283027	0.000019	9.0	15.7	0.68	310	317	321	−0.98
10	0.001285	0.027472	0.282959	0.000025	6.6	13.2	0.88	310	418	481	−0.96
13	0.001269	0.027982	0.282973	0.000024	7.1	13.7	0.85	310	399	450	−0.96
15	0.000847	0.021381	0.283026	0.000025	9.0	15.6	0.88	310	318	324	−0.97
18	0.001195	0.027904	0.283013	0.000023	8.5	15.1	0.82	310	340	358	−0.96
27	0.001273	0.028204	0.283013	0.000025	8.5	15.1	0.87	310	341	359	−0.96
Pyroxene basalt (CJSH-2)											
1	0.001174	0.061791	0.282979	0.000033	7.3	13.9	1.17	313	390	434	−0.96
6	0.001626	0.073112	0.282870	0.000029	3.5	10.0	1.02	313	552	686	−0.95
8	0.001166	0.056909	0.282829	0.000031	2.0	8.67	1.09	313	602	771	−0.96
11	0.001204	0.066397	0.282958	0.000029	6.6	13.2	1.04	313	419	481	−0.96
16	0.002461	0.109072	0.283013	0.000038	8.5	14.9	1.34	313	352	373	−0.93
20	0.000899	0.040552	0.282811	0.000025	1.4	8.06	0.89	313	624	810	−0.97

the $\varepsilon Nd(t)$ versus $(Nd/Hf)_{PM}$ diagram (Fig. 11; Tang *et al.* 2013). The results show that the primary magma underwent < 5 % slab-derived fluid metasomatism in the mantle source.

Based on Nd–Sr–Pb and Hf isotope systematics, the mantle source of the studied tholeiitic rocks can be further limited. The basaltic rocks have high positive $\varepsilon Nd(t)$ (+4.21 to +4.36) and $\varepsilon Hf(t)$ (+13.0 on average) values, indicating their N-MORB-like depleted mantle features (Fig. 12a, b). It should be noted that the relatively high initial $^{87}Sr/^{86}Sr$ ratios make the plots of the basaltic samples deviate away from the mantle array in the Nd–Sr isotope diagram (Fig. 12a), probably suggesting the incorporation of Sr from seawater in the source (Lin *et al.* 2019). In the $^{207}Pb/^{204}Pb$ and $^{208}Pb/^{204}Pb$ versus $^{206}Pb/^{204}Pb$ diagrams (Fig. 12c, d), all the basaltic samples plotted in the Indian MORB field (Kempton *et al.* 2002), consistent with the Nd–Hf isotope characteristics. Notably, the Sr–Nd isotopes of the basaltic rocks are similar to those of Early Carboniferous subduction-related volcanic rocks in the Miaoergou and Karamary areas (*c.* 331–344 Ma; Geng *et al.* 2011) and BABB in Hatu area (*c.* 324 Ma; Shen *et al.* 2013) of southern West Junggar (Fig. 12a), probably suggesting their genetic affinities.

A more useful approach to the mantle source nature is the use of plots of incompatible elements and their ratios. As shown in the Sm/Yb versus Sm and Sm/Yb versus La/Sm diagrams (Fig. 13; Aldanmaz *et al.* 2000), all the samples plotted on the spinel lherzolite partial melting curve, which shows that the samples were formed by ~5–10 % partial melting of a spinel lherzolite facies mantle source. Additionally, the low $(Gd/Yb)_N$, $(Dy/Yb)_N$ and La/Yb ratios (1.05–1.50, 1.06–1.17 and 1.21–1.49, respectively) and relatively high HREE concentrations (14.5–18.0 ppm; > 15 times chondrite) of the basaltic rocks further imply that these rocks originated from partial melting of spinel lherzolite mantle (Chung, 1999). Therefore, we infer that the generation of the parental magmas of the basaltic rocks in the Chengjisihanshan Formation were most likely derived from ~5–10 % partial melting of a depleted spinel lherzolitic mantle source metasomatized by < 5 % slab-derived fluids.

5.c. Tectonic setting and geological significance

It is generally believed that the mafic magmas possessing both MORB-like and arc-like compositional characteristics formed in
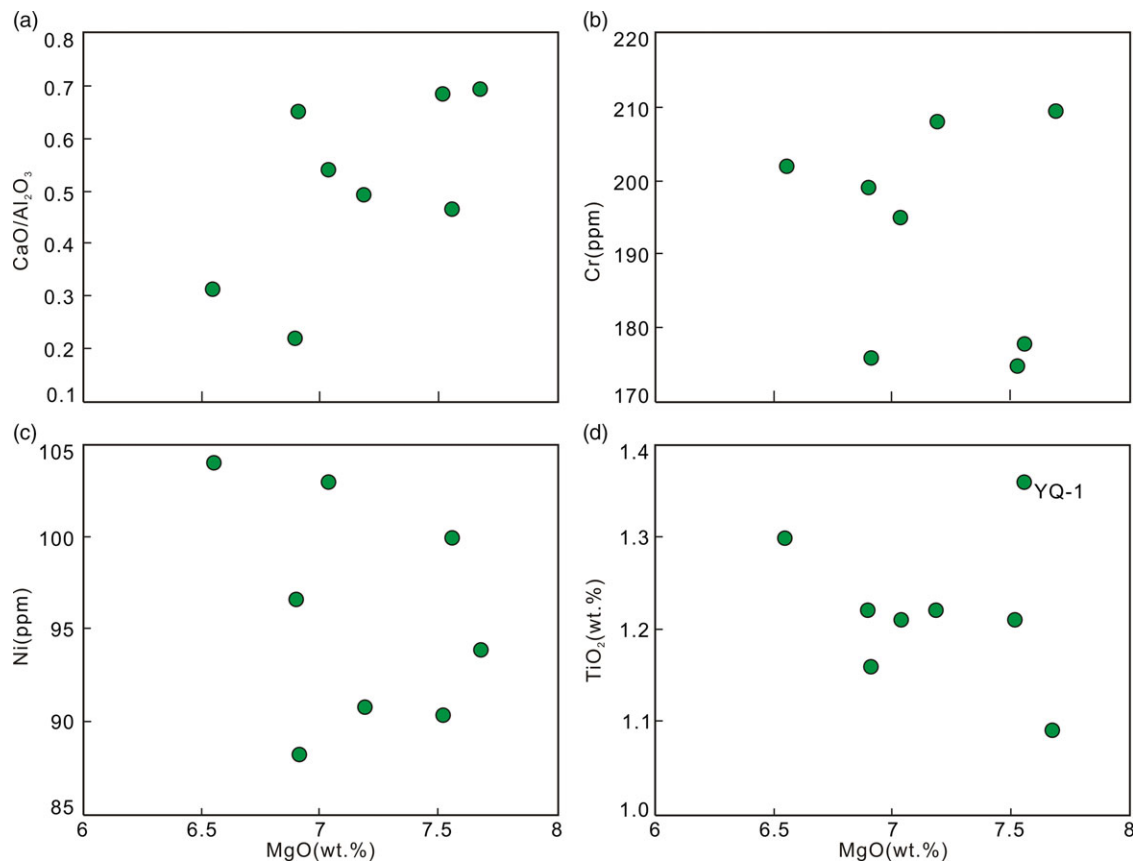
Fig. 10. (Colour online) Plots of selected elements and their ratios for the basaltic rocks.
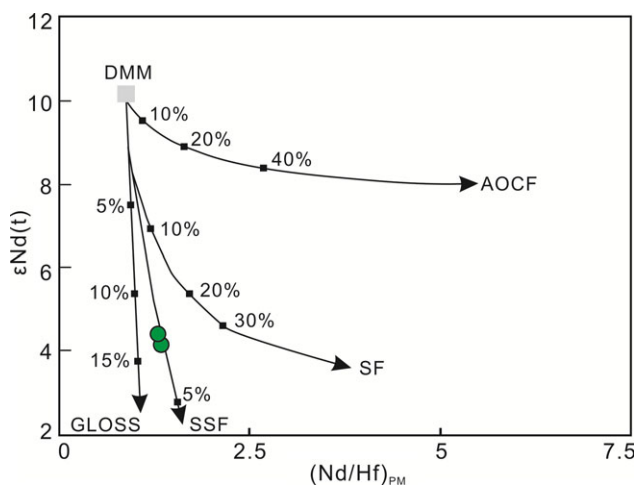

Fig. 11. (Colour online) Plots of εNd(t) versus (Nd/Hf)$_{PM}$ (after Tang *et al.* 2013) for the basaltic rocks. DMM – depleted mantle-derived melt; AOCF – altered oceanic crust fluid; GLOSS – global subducting sediment; SF – slab fluid; SSF – subducted sediment fluid.

a fore-arc basin or back-arc basin above the subduction zone (e.g. Gribble *et al.* 1996; Shinjo *et al.* 1999; Taylor & Martinez, 2003; Reagan *et al.* 2010); therefore, data for the Okinawa BABB from a typical modern intra-continental back-arc basin (Shinjo *et al.* 1999), the Mariana BABB from a typical modern intra-oceanic back-arc basin (Pearce *et al.* 2005) and the Early Carboniferous Hatu BABB in southern West Junggar

(*c.* 324 Ma; Shen *et al.* 2013) as well as the Mariana fore-arc basin basalt (FAB) (Reagan *et al.* 2010) were added to Figures 8 and 9 for comparison. The results show that the tholeiitic rocks from the Chengjisihanshan Formation are analogous to those of the Mariana BABB (Pearce *et al.* 2005) and Hatu BABB (Shen *et al.* 2013) both in major- and trace-element compositional aspects, but differ from those of the Okinawa BABB (Shinjo *et al.* 1999) and Mariana FAB (Reagan *et al.* 2010) (Figs 8, 9). Additionally, the asthenospheric MORB-type mantle occurring in a fore-arc basin would likely be characterized by high oxygen fugacity, transforming vanadium into a high valence form with strong incompatibility, and partial melting of this mantle would yield relatively low Ti/V ratios (Shervais, 1982; Reagan *et al.* 2010). However, the basaltic rocks in this study yielded Ti/V ratios (25.9–27.9) much higher than those of typical FAB (15.3–16.4; Reagan *et al.* 2010) but comparable to BABB from the Mariana Trough (16.8–34.9; Pearce *et al.* 2005). Moreover, our samples also have similar (La/Yb)$_N$ (0.87–1.07), Sm/Nd (0.32–0.35), Th/Yb (0.10–0.13) and Th/Nb (0.10–0.12) ratios to those from the Mariana Trough (Pearce *et al.* 2005).

More importantly, trace and body fossils together with turbidites clearly reveal a deep-sea to littoral shallow marine environment in West Junggar during Late Carboniferous time (e.g. Li & Jin, 1989; Jin & Li, 1998). In addition, regional palaeogeographic and geological study similarly indicates that the northern Xinjiang region still remained an active continental margin until Late Carboniferous to Early Permian times (Xiao *et al.* 2008). Furthermore, the Upper Carboniferous Chengjisihanshan Formation in the Aletunzhawati area consists of tuffaceous
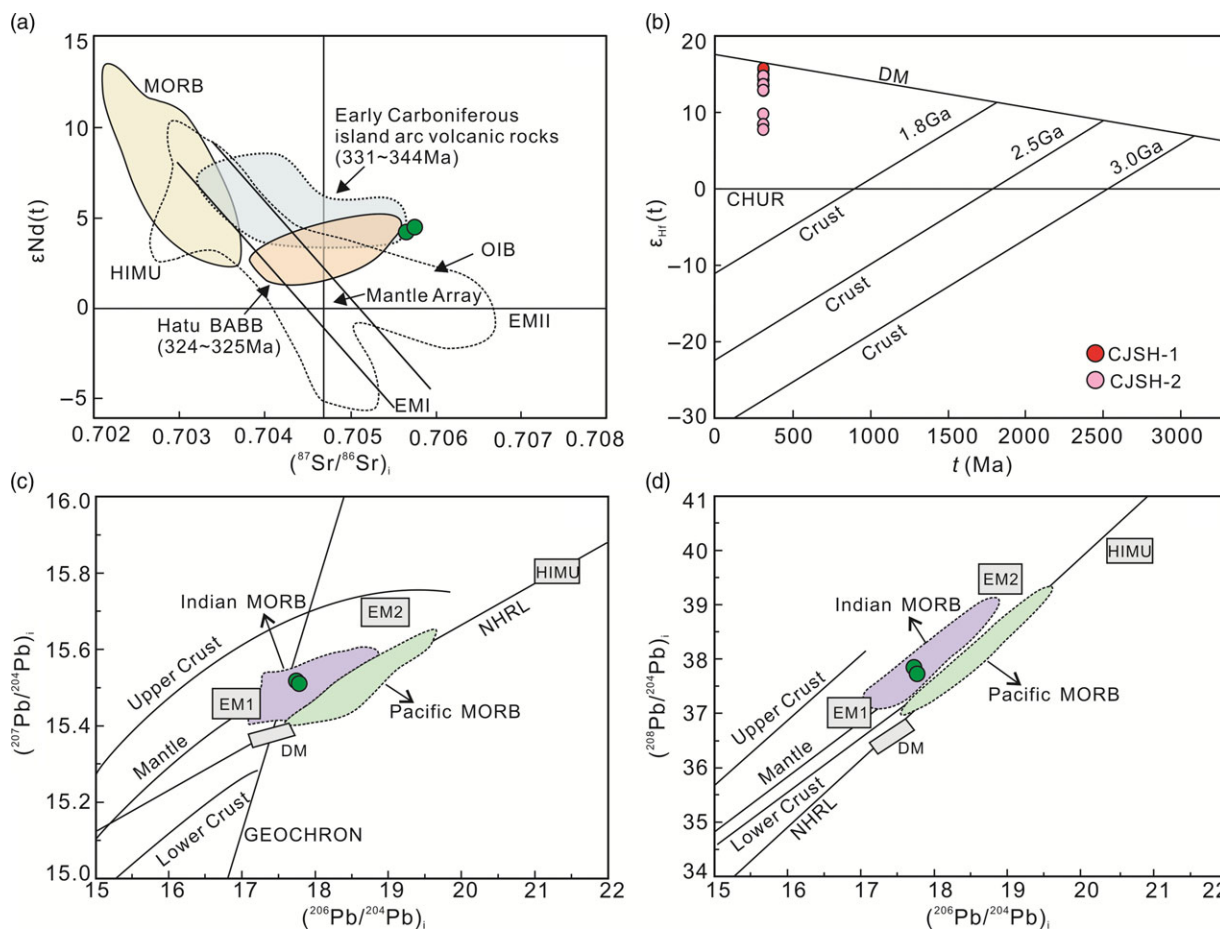
Fig. 12. (Colour online) (a) Sr–Nd, (b) zircon Hf, and (c, d) Pb isotopic compositions for the basaltic rocks. Data for the Hatu BABB are from Shen *et al*. (2013), for the Early Carboniferous island arc volcanic rocks in southern West Junggar are from Geng *et al*. (2011), and for the Indian MORB and Pacific MORB are from Kempton *et al*. (2002). CHUR – chondritic uniform reservoir; DM – depleted mantle; EMI/1 – enriched mantle I; EMII/2 – enriched mantle II; HIMU – high μ; MORB – mid-ocean ridge basalt; NHRL – Northern Hemisphere Reference Line; OIB – ocean island basalt.
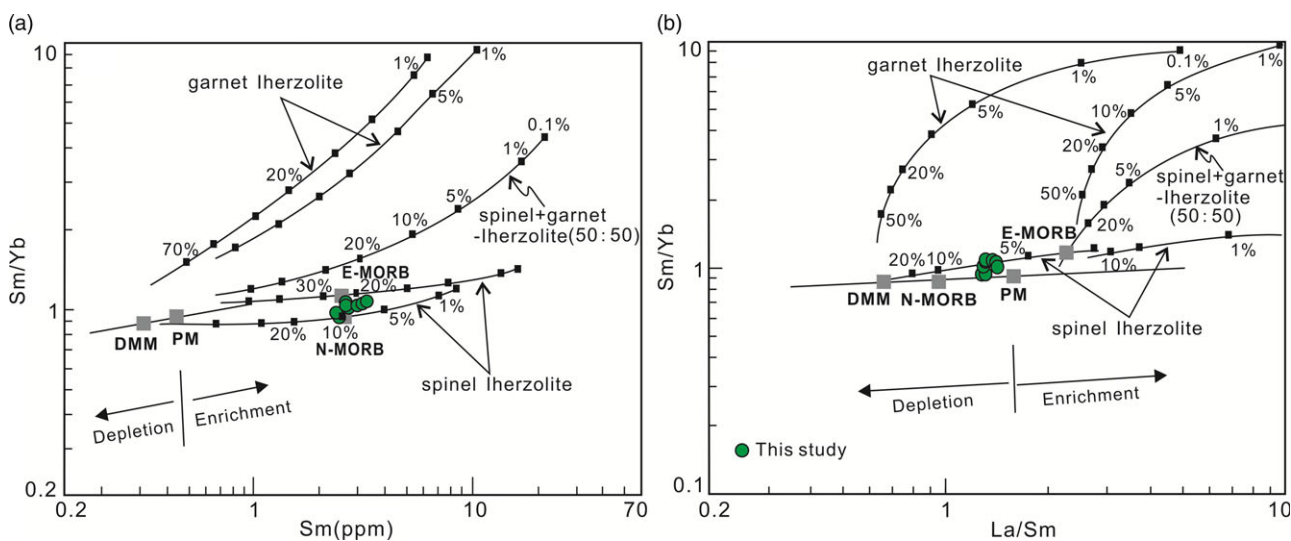
Fig. 13. (Colour online) (a) Plots of Sm/Yb–Sm and (b) Sm/Yb–La/Sm (after Aldanmaz *et al*. 2000) for the basaltic rocks. DMM – depleted MORB mantle; E-MORB – enriched mid-ocean ridge basalt; N-MORB – normal mid-ocean ridge basalt; PM – primitive mantle.
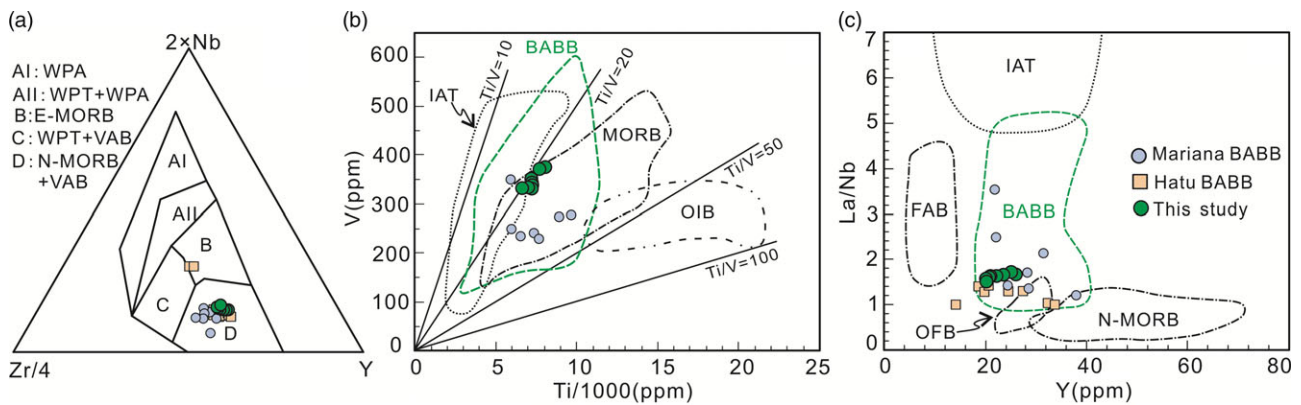
Fig. 14. (Colour online) Tectonic setting discrimination diagrams with trace elemental plots for the basaltic rocks in the Chengjisihanshan Formation. (a) 2*Nb–Zr/4–Y (after Meschede, 1986); (b) V–Ti/1000 (after Shervais, 1982); (c) La/Nb–Y (after Floyd *et al*. 1991). Data for the Mariana BABB are from Pearce *et al*. (2005) and for the Hatu BABB are from Shen *et al*. (2013). IAT – island arc tholeiites; OFB – ocean floor basalt; VAB – volcanic arc basalt; WPA – within-plate alkali basalt; WPT – within-plate tholeiitic basalt.
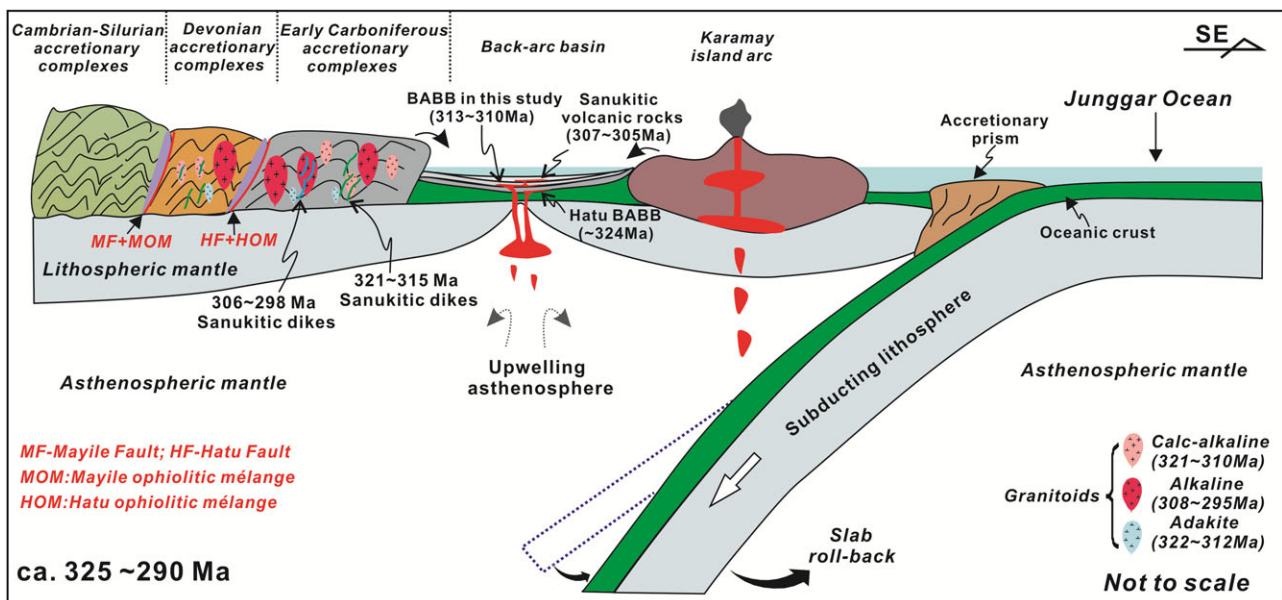
Fig. 15. (Colour online) Schematic map showing the tectonic setting of the Late Carboniferous to Early Permian period (*c*. 325–290 Ma) in southern West Junggar (modified after Duan *et al*. 2019). Age data shown in this figure are from Chen & Arakawa (2005), Han *et al*. (2006), Geng *et al*. (2009), Gao *et al*. (2014), Shen *et al*. (2009, 2012, 2013), Tang *et al*. (2010, 2012), Yin *et al*. (2010, 2013, 2015), Duan *et al*. (2015, 2018*a*,*b*,*c*, 2019), Li *et al*. (2017).

siltstones, tuffaceous sandstones, feldspar lithic sandstones, lenticular limestone containing marine fossils, and a minor amount of pebbly sandstones and conglomerates with intercalated beds of chert and basalt in the field (Fig. 2b), indicating the existence of an oceanic basin in Late Carboniferous time. The aforementioned geochemical data and the above lines of geological evidence jointly suggest that the studied basaltic rocks were more likely generated in a back-arc basin setting, which is also consistent with the plots of 2*Nb–Zr/4–Y (Fig. 14a; Meschede, 1986), V–Ti/1000 (Fig. 14b; Shervais, 1982) and La/Nb–Y (Fig. 14c; Floyd *et al*. 1991). On the basis of this study and taking previous interpretations into consideration, we here prefer to suggest that the studied Late Carboniferous tholeiitic rocks from the Chengjisihanshan Formation in the Aletunzhawati area were formed in an intra-oceanic back-arc basin tectonic setting (Fig. 15). The identification of Late Carboniferous BABB in the Chengjisihanshan Formation indicates that the arc-basin evolutionary system during late Early Carboniferous time (~324 Ma; Shen *et al*. 2013) continued

until 310 Ma in southern West Junggar, and the Junggar Ocean likely closed after Late Carboniferous time.

The Carboniferous is a crucial period for the tectonic transition of West Junggar. Massive Carboniferous–Permian magmatic rocks are extensively distributed in the southern part, which provide favourable material conditions for understanding the characteristics of Late Palaeozoic magmatic activities and the tectonic evolution of the Junggar Ocean. In the recent tectonic models, West Junggar has been linked to multiple intra-oceanic accretionary episodes from Devonian to Late Carboniferous time (e.g. Xiao *et al*. 2008; Zhang *et al*. 2011*b*; Li *et al*. 2017; Duan *et al*. 2018*c*, 2019). During Early Carboniferous time, a large number of volcanic rocks generated in the subduction process have been reported in southern West Junggar, such as Nb-enriched arc basalts found in the Barleik Mountain area (~349 Ma; Li *et al*. 2014), island arc volcanic rocks distributed throughout the Miaoergou–Baijiantan region (~344 Ma; Geng *et al*. 2011) and oceanic island basalts formed by upwelling of asthenospheric mantle

through a slab window in a fore-arc setting in the northern Karamay region during consumption of the West Junggar Ocean (~345 Ma; Yang *et al.* 2016). These special rock associations indicate that there should be a subduction-dominated setting in southern West Junggar during Early Carboniferous time. The discovery of *c.* 324 Ma BABB in the Hatu area (Shen *et al.* 2013) suggests that a back-arc extensional setting occurred in southern West Junggar at the end of Early Carboniferous time.

In the early to middle stage of Late Carboniferous time, as consumption of the Junggar oceanic lithosphere proceeded, subduction-related intermediate-acid intrusive rocks were widely distributed in southern West Junggar, such as *c.* 322–312 Ma slab-derived adakitic rocks exposed in the Baogutu, Dulunhe and Huangliangzi regions (Zhang *et al.* 2006; Shen *et al.* 2009, 2012; Tang *et al.* 2010; Duan *et al.* 2015, 2018*b*), and contemporaneous sanukitic dykes from the Bieluagaxi and Karamay regions (*c.* 321–315 Ma; Yin *et al.* 2010; Duan *et al.* 2019), as well as calc-alkaline I-type granitic stocks distributed on both sides of the Darbut Fault (*c.* 319–310 Ma; e.g. Tang *et al.* 2012; Duan *et al.* 2018*a*). The confirmation of *c.* 313–310 Ma intra-oceanic BABB in this study indicates that a remnant oceanic basin under an extensional environment still occurred in southern West Junggar during the middle stage of Late Carboniferous time. Thereafter, volcanic rocks sharing some affinities with sanukitoids were erupted in Hala'alate Mountain (*c.* 307–305 Ma; Li *et al.* 2017), and contemporaneously, massive dioritic dykes carrying sanukitoid compositions were widely distributed in the Miaoergou region (*c.* 306–298 Ma; Yin *et al.* 2013, 2015; Duan *et al.* 2018*c*); voluminous alkaline A-type granitic batholiths (*c.* 308–295 Ma; e.g. Chen & Arakawa, 2005; Han *et al.* 2006; Geng *et al.* 2009; Gao *et al.* 2014) were also generated in the Devonian–Early Carboniferous accretionary complexes (Fig. 15).

6. Conclusions

(1) The basaltic rocks from the Chengjisihanshan Formation in southern West Junggar were formed in Late Carboniferous time (*c.* 313–310 Ma).

(2) The basaltic rocks are tholeiitic and exhibit both N-MORB-like and arc-like geochemical signatures, and were likely derived from ~5–10 % partial melting of a depleted spinel lherzolitic mantle source metasomatized by < 5 % slab-derived fluids within an intra-oceanic back-arc basin setting.

(3) An arc-basin evolutionary system still existed in southern West Junggar at *c.* 310 Ma, and the Junggar Ocean closed after Late Carboniferous time.

References

Aldanmaz E, Pearce JA, Thirlwall MF and Mitchell JG (2000) Petrogenetic evolution of late Cenozoic, post-collision volcanism in western Anatolia, Turkey. *Journal of Volcanology and Geothermal Research* **102**, 67–95.

Babinski M, VanSchmus WR and Chemale JF (1999) Pb–Pb dating and Pb isotope geochemistry of Neoproterozoic carbonate rocks from the São Francisco basin, Brazil: implications for the mobility of Pb isotopes during tectonism and metamorphism. *Chemical Geology* **160**, 175–99.

BGMRXUAR (Bureau of Geology and Mineral Resources of Xinjiang Uygur Autonomous Region) (1993) *Regional Geology of Xinjiang Uygur Autonomous Region.* Beijing: Geological Publishing House, 841 pp. (in Chinese with English abstract).

Belousova EA, Griffin WL, O'Reilly SY and Fisher NI (2002) Igneous zircon: trace element composition as an indicator of source rock type. *Contributions to Mineralogy and Petrology* **143**, 602–22.

Blichert-Toft J and Albarède F (1997) The Lu–Hf isotope geochemistry of chondrites and the evolution of the mantle-crust system. *Earth and Planetary Science Letters* **148**, 243–58.

Chen B and Arakawa Y (2005) Elemental and Nd–Sr isotopic geochemistry of granitoids from the West Junggar foldbelt (NW China), with implications for Phanerozoic continental growth. *Geochimica et Cosmochimica Acta* **69**, 1307–20.

Choulet F, Faure M, Cluzel D, Chen Y, Lin W and Wang B (2012) From oblique accretion to transpression in the evolution of the Altaid collage: new insights from West Junggar, northwestern China. *Gondwana Research* **21**, 530–47.

Chu NC, Taylor RN, Chavagnae V, Nesbitt RW, Boela RM, Milton JA, German CR, Bayon G and Burton K (2002) Hf isotope ratio analysis using multi-collector inductively coupled plasma mass spectrometry: an evaluation of isobaric interference corrections. *Journal of Analytical Atomic Spectrometry* **17**, 1567–74.

Chung SL (1999) Trace element and isotope characteristics of Cenozoic basalts around the Tanlu Fault with implications for the eastern plate boundary between North and South China. *The Journal of Geology* **107**, 301–12.

Corfu F, Hanchar JM, Hoskin PW and Kinny P (2003) Atlas of zircon textures. *Reviews in Mineralogy and Geochemistry* **53**, 469–500.

Duan FH, Li YJ, Wang R, Ji ZB, Cheng WL and Guo X (2015) Characteristics and geological significance of adakitic rocks of the Dulunhe granite in Toli, Western Junggar. *Journal of Mineralogy and Petrology* **35**, 8–16 (in Chinese with English abstract).

Duan FH, Li YJ, Wang R, Zhi Q, Chao WD and Ma YL (2018a) LA-ICP-MS zircon U–Pb geochronology, geochemical characteristics of Tasikuola granite in Western Junggar, Xinjiang and its geological significance. *Acta Geologica Sinica* **92**, 1401–17 (in Chinese with English abstract).

Duan FH, Li YJ, Yang GX, Zhi Q, Li YH, Tao XY, Gao JB and Chen RG (2018b) Late Carboniferous adakitic porphyries in the Huangliangzi pluton, West Junggar (Xinjiang), NW China: petrogenesis and their tectonic implications. *Geological Journal* **53**, 97–113.

Duan FH, Li YJ, Zhi Q, Wan Y and Ren Y (2018c) Geochemical characteristics, petrogenesis mechanism of the sanukitic dikes in Miaoergou and their significance in West Junggar, Xinjiang, NW China. *Geotectonica et Metallogenia* **42**, 759–76 (in Chinese with English abstract).

Duan FH, Li YJ, Zhi Q, Yang GX and Gao JB (2019) Petrogenesis and geodynamic implications of Late Carboniferous sanukitic dikes from the Bieluagaxi area of West Junggar, NW China. *Journal of Asian Earth Sciences* **175**, 158–77.

Feng YM, Coleman RG, Tilton G and Xiao XC (1989) Tectonic evolution of the West Junggar region, Xinjiang, China. *Tectonics* **8**, 729–52.

Floyd PA, Kelling G, Gökçen SL and Gökçen N (1991) Geochemistry and tectonic environment of basaltic rocks from the Misis ophiolitic mélange, south Turkey. *Chemical Geology* **89**, 263–80.

Gao R, Xiao L, Pirajno F, Wang GC, He XX, Yang G and Yan SW (2014) Carboniferous–Permian extensive magmatism in the West Junggar, Xinjiang, northwestern China: its geochemistry, geochronology, and petrogenesis. *Lithos* **204**, 125–43.

Geng HY, Sun M, Yuan C, Xiao WJ, Xian WS, Zhao GC, Zhang LF, Wong K and Wu FY (2009) Geochemical, Sr–Nd and zircon U–Pb–Hf isotopic studies of Late Carboniferous magmatism in the West Junggar, Xinjiang: implications for ridge subduction? *Chemical Geology* **266**, 364–89.

Geng HY, Sun M, Yuan C, Zhao GC and Xiao WJ (2011) Geochemical and geochronological study of early Carboniferous volcanic rocks from the West Junggar: petrogenesis and tectonic implications. *Journal of Asian Earth Sciences* **42**, 854–66.

Gribble RF, Stern RJ, Bloomer SH, Stüben D, O'Hearn T and Newman S (1996) MORB mantle and subduction components interact to generate basalts in the southern Mariana Trough back-arc basin. *Geochimica et Cosmochimica Acta* **60**, 2153–66.

Gu PY, Li YJ, Zhang B, Tong LL and Wang JN (2009) LA-ICP-MS zircon U–Pb dating of gabbro in the Darbut ophiolite, western Junggar, China. *Acta Petrologica Sinica* **25**, 1364–72 (in Chinese with English abstract).

Guo LS, Liu YL, Wang ZH, Song D, Xu FJ and Su L (2010) The zircon U–Pb LA-ICP-MS geochronology of volcanic rocks in Baogutu areas, western Junggar. *Acta Petrologica Sinica* **26**, 471–7 (in Chinese with English abstract).

Han BF, Ji JQ, Song B, Chen LH and Zhang L (2006) Late Paleozoic vertical growth of continental crust around the Junggar basin, Xinjiang, China (Part I): timing of post-collisional plutonism. *Acta Petrologica Sinica* **22**, 1077–86 (in Chinese with English abstract).

Hawkesworth CJ, Turner SP, McDermott F, Peate DW and Van Calsteren P (1997) U–Th isotopes in arc magmas: implications for element transfer from the subducted crust. *Science* **276**, 551–5.

Hémond C, Hofmann AW, Vlastélic I and Nauret F (2006) Origin of MORB enrichment and relative trace element compatibilities along the Mid-Atlantic Ridge between 10° and 24°N. *Geochemistry, Geophysics, Geosystems* **7**, Q12010. doi: 10.1029/2006GC001317.

Hofmann AW, Jochum KP, Seufert M and White WM (1986) Nb and Pb in oceanic basalts: new constraints on mantle evolution. *Earth and Planetary Science Letters* **79**, 33–45.

Jahn BM, Windley B, Natal'in B and Dobretsov N (2004) Phanerozoic continental growth in Central Asia. *Journal of Asian Earth Sciences* **23**, 599–603.

Jahn BM, Wu FY and Chen B (2000) Massive granitoid generation in Central Asia, Nd isotope evidence and implication for continental growth in the Phanerozoic. *Episodes* **23**, 82–92.

Jin HJ and Li YC (1998) Study on the Carboniferous biogenic sedimentary structure in the northwestern margin of Junggar Basin. *Chinese Science Bulletin* **43**, 1888–91 (in Chinese).

Kempton PD, Pearce JA, Barry TL, Fitton JG, Langmuir C and Christie DM (2002) Sr–Nd–Pb–Hf isotope results from ODP Leg 187: evidence for mantle dynamics of the Australian–Antarctic discordance and origin of the Indian MORB source. *Geochemistry, Geophysics, Geosystems* **3**, 1–35.

Klein EM and Karsten JL (1995) Ocean-ridge basalts with convergent-margin geochemical affinities from the Chile Ridge. *Nature* **374**, 52–7.

Lassiter JC and DePaolo DJ (1997) Plume/lithosphere interaction in the generation of continental and oceanic flood basalts: chemical and isotopic constraints. In *Large Igneous Provinces: Continental, Oceanic, and Planetary Flood Volcanism* (eds JJ Mahoney and MF Coffin), pp. 335–56. American Geophysical Union, Geophysical Monograph vol. 100. Washington, DC, USA.

Li GY, Li YJ, Wang XC, Yang GX, Wang R, Xiang KP, Liu J and Tong LL (2017) Identifying late Carboniferous sanukitoids in Hala'alate Mountain, Northwest China: new constraint on the closing time of remnant ocean basin in West Junggar. *International Geology Review* **59**, 1116–30.

Li JY and Jin HJ (1989) The trace fossils discovery and its environment significance in Carboniferous turbidite series, the northwest border of Zhunga'er basin, Xinjiang. *Scientia Geologica Sinica* **63**, 9–15 (in Chinese with English abstract).

Li YJ, Shen R, Wang R, Guo ST, Tong LL and Yang GX (2014) Discovery and significance of Early Carboniferous Nb-enriched basalts in Barnuke, West Junggar, Xinjiang. *Acta Petrologica Sinica* **30**, 3501–11 (in Chinese with English abstract).

Li YJ, Tong LL, Zhang B, Liu J, Zhang TJ and Wang JN (2010) On the old and new relationship between Xibeikulasi Formation and Baogutu Formation of the Carboniferous system, West Junggar. *Xinjiang Geology* **28**, 130–6 (in Chinese with English abstract).

Lin ZF, Yuan C, Zhang YY, Sun M, Long XP, Wang XY and Huang ZY (2019) Triassic depleted lithospheric mantle underneath the Paleozoic Chinese Altai orogen: evidence from MORB-like basalts. *Journal of Asian Earth Sciences* **185**, 104021. doi: 10.1016/j.jseaes.2019.104021.

Liu B, Han BF, Gong EP and Chen JF (2019) The tectono-magmatic evolution of the West Junggar terrane (NW China) unravelled by U–Pb ages of detrital zircons in modern river sands. *International Geology Review* **61**, 607–21.

Ludwig KR (2003) *Isoplot/Ex Version 2.49. A Geochronological Toolkit for Microsoft Excel.* Berkeley: Berkeley Geochronology Center Special Publication no.1a, 56 pp.

Lugmair GW and Marti K (1978) Lunar initial ^{143}Nd/^{144}Nd: differential evolution of the lunar crust and mantle. *Earth and Planetary Science Letters* **39**, 349–57.

Marques LS, Dupré B and Piccirillo EM (1999) Mantle source compositions of the Paraná Magmatic Province (southern Brazil): evidence from trace element and Sr–Nd–Pb isotope geochemistry. *Journal of Geodynamics* **28**, 439–58.

Meschede M (1986) A method of discriminating between different types of mid-ocean ridge basalts and continental tholeiites with the Nb–Zr–Y diagram. *Chemical Geology* **56**, 207–18.

Miyashiro A (1974) Volcanic rock series in island arcs and active continental margins. *American Journal of Science* **274**, 321–55.

Naumann TR and Geist DJ (1999) Generation of alkalic basalt by crystal fractionation of tholeiitic magma. *Geology* **27**, 423–6.

Pearce JA and Peate DW (1995) Tectonic implications of the composition of volcanic arc magmas. *Annual Review of Earth and Planetary Sciences* **23**, 251–85.

Pearce JA, Stern RJ, Bloomer SH and Fryer P (2005) Geochemical mapping of the Mariana arc-basin system: implications for the nature and distribution of subduction components. *Geochemistry, Geophysics, Geosystems* **6**, Q07006. doi: 10.1029/2004GC000895.

Perfit MR, Gust DA, Bence AE, Arculus RJ and Taylor SR (1980) Chemical characteristics of island-arc basalts: implications for mantle sources. *Chemical Geology* **30**, 227–56.

Plank T (2005) Constraints from thorium/lanthanum on sediment recycling at subduction zones and the evolution of the continents. *Journal of Petrology* **46**, 921–44.

Rapp RP and Watson EB (1995) Dehydration melting of metabasalt at 8–32 kbar: implications for continental growth and crust-mantle recycling. *Journal of Petrology* **36**, 891–931.

Reagan MK, Ishizuka O, Stern RJ, Kelley KA, Ohara Y, Blichert-toft J, Bloomer SH, Cash J, Fryer P and Hanan BB (2010) Fore-arc basalts and subduction initiation in the Izu-Bonin-Mariana system. *Geochemistry, Geophysics, Geosystems* **11**, Q03X12. doi: 10.1029/2009GC002871.

Sato K, Tassinari CGC, Kawashita K and Petronillo L (1995) Método geocronológico Sm–Nd no IG/USP e suas aplicações. *Anais Da Academia Brasileira De Ciências* **67**, 313–36.

Scherer E, Münker C and Mezger K (2001) Calibration of the lutetium-hafnium clock. *Science* **293**, 683–7.

Shen P, Pan HD, Xiao WJ, Li XH, Dai HW and Zhu HP (2013) Early Carboniferous intra-oceanic arc and back-arc basin system in the West Junggar, NW China. *International Geology Review* **55**, 1991–2007.

Shen P, Shen YC, Liu TB, Meng L, Dai HW and Yang YH (2009) Geochemical signature of porphyries in the Baogutu porphyry copper belt, western Junggar, NW China. *Gondwana Research* **16**, 227–42.

Shen P, Shen YC, Pan HD, Li XH, Dong LH, Wang JB, Zhu HP, Dai HW and Guan WN (2012) Geochronology and isotope geochemistry of the Baogutu porphyry copper deposit in the West Junggar region, Xinjiang, China. *Journal of Asian Earth Sciences* **49**, 99–115.

Shervais JW (1982) Ti–V plots and the petrogenesis of modern and ophiolitic lavas. *Earth and Planetary Science Letters* **59**, 101–18.

Shinjo R, Chung SL, Kato Y and Kimura M (1999) Geochemical and Sr–Nd isotopic characteristics of volcanic rocks from the Okinawa Trough and Ryukyu Arc: implications for the evolution of a young, intracontinental back arc basin. *Journal of Geophysical Research* **104**, 10591–608.

Steiger RH and Jäger E (1977) Subcommission on geochronology: convention on the use of decay constants in geo- and cosmochronology. *Earth and Planetary Science Letters* **36**, 359–62.

Sun SS and McDonough WF (1989) Chemical and isotopic systematics of oceanic basalts: Implications for mantle composition and processes. In *Magmatism in Ocean Basins* (AD Saunders and MJ Norry), pp. 313–45. Geological Society of London, Special Publication no. 42.

Tang DM, Qin KZ, Su BX, Sakyi PA, Liu YS, Mao Q, Santosh M and Ma YG (2013) Magma source and tectonics of the Xiangshanzhong mafic-ultramafic intrusion in the Central Asian Orogenic Belt, NW China, traced from geochemical and isotopic signatures. *Lithos* **170**, 144–63.

Tang GJ, Wang Q, Wyman DA, Li ZX, Zhao ZH, Jia XH and Jiang ZQ (2010) Ridge subduction and crustal growth in the Central Asian Orogenic Belt: evidence from Late Carboniferous adakites and high-Mg diorites in the western Junggar region, northern Xinjiang (West China). *Chemical Geology* **277**, 281–300.

Tang GJ, Wang Q, Wyman DA, Li ZX, Zhao ZH and Yang YH (2012) Late Carboniferous high εNd(t)–εHf(t) granitoids, enclaves and dikes in western Junggar, NW China: ridge-subduction-related magmatism and crustal growth. *Lithos* **140–141**, 86–102.

Taylor B and Martinez F (2003) Back-arc basin basalt systematics. *Earth and Planetary Science Letters* **210**, 481–97.

Vervoot JD and Blichert-Toft J (1999) Evolution of the depleted mantle: Hf isotope evidence from juvenile rocks through time. *Geochimica et Cosmochimica Acta* **63**, 533–56.

Wasserburg GJ, Jacobsen SB, DePaolo DJ, McCulloch MT and Wen T (1981) Precise determination of SmNd ratios, Sm and Nd isotopic abundances in standard solutions. *Geochimica et Cosmochimica Acta* **45**, 2311–23.

Winchester JA and Floyd PA (1977) Geochemical discrimination of different magma series and their differentiation products using immobile elements. *Chemical Geology* **20**, 325–43.

Windley BF, Alexeiev D, Xiao WJ, Kroner A and Badarch G (2007) Tectonic models for accretion of the Central Asian Orogenic Belt. *Journal of the Geological Society, London* **164**, 31–47.

Windley BF and Xiao WJ (2018) Ridge subduction and slab windows in the Central Asian Orogenic Belt: tectonic implications for the evolution of an accretionary orogen. *Gondwana Research* **61**, 73–87.

Woodhead JD, Hergt JM, Davidson JP and Eggins SM (2001) Hafnium isotope evidence for 'conservative' element mobility during subduction zone processes. *Earth and Planetary Science Letters* **192**, 331–46.

Xiang KP, Li YJ, Xu L, Zhang HW and Tong LL (2013) The definition of Chengjisihanshan Formation and its significances in Baijiantan region, West Junggar, Xinjiang. *Northwestern Geology* **46**, 63–8 (in Chinese with English abstract).

Xiao WJ, Han CM, Yuan C, Sun M, Lin SF, Chen HL, Li ZL, Li JL and Sun S (2008) Middle Cambrian to Permian subduction-related accretionary orogenesis of Northern Xinjiang, NW China: implications for the tectonic evolution of central Asia. *Journal of Asian Earth Sciences* **32**, 102–17.

Xiao WJ and Santosh M (2014) The western Central Asian Orogenic Belt: a window to accretionary orogenesis and continental growth. *Gondwana Research* **25**, 1429–44.

Xu Z, Han BF, Ren R, Zhou YZ, Zhang L, Chen JF, Su L, Li XH and Liu DY (2012) Ultramafic-mafic mélange, island arc and post-collisional intrusions in the Mayile Mountain, West Junggar, China: implications for Paleozoic intra-oceanic subduction-accretion process. *Lithos* **132**, 141–61.

Yang GX, Li YJ, Santosh M, Gu PY, Yang BK, Zhang B, Wang HB, Zhong X and Tong LL (2012) A Neoproterozoic seamount in the Paleoasian Ocean: Evidence from zircon U–Pb geochronology and geochemistry of the Mayile ophiolitic mélange in West Junggar, NW China. *Lithos* **140–141**, 53–65.

Yang GX, Li YJ, Tong LL, Li GY, Wu L and Wang ZP (2016) Petrogenesis and tectonic implications of early Carboniferous alkaline volcanic rocks in Karamay region of West Junggar, Northwest China. *International Geology Review* **58**, 1278–93.

Yin JY, Chen W, Xiao WJ, Yuan C, Sun M, Tang GJ, Yu S, Long XP, Cai KD, Geng HY, Zhang Y and Liu XY (2015) Petrogenesis of Early-Permian sanukitoids from West Junggar, northwest China: implications for later Paleozoic crustal growth in Central Asia. *Tectonophysics* **662**, 385–97.

Yin JY, Long XP, Yuan C, Sun M, Zhao GC and Geng HY (2013) A Late Carboniferous–Early Permian slab window in the West Junggar of NW China: geochronological and geochemical evidence from mafic to intermediate dikes. *Lithos* **175–176**, 146–62.

Yin JY, Yuan C, Sun M, Long XP, Zhao GC, Wong KP, Geng HY and Cai KD (2010) Late Carboniferous high-Mg dioritic dikes in western Junggar, NW China: geochemical features, petrogenesis and tectonic implications. *Gondwana Research* **17**, 145–52.

Zhang LC, Wan B, Jiao XJ and Zhang R (2006) Characteristics and geological significance of adakitic rocks in copper-bearing porphyry in Baogutu, western Junggar. *Geology in China* **33**, 626–31 (in Chinese with English abstract).

Zhang JE, Xiao WJ, Han CM, Ao SJ, Yuan C, Sun M, Geng HY, Zhao GC, Guo QQ and Ma C (2011a) Kinematics and age constraints of deformation in a Late Carboniferous accretionary complex in Western Junggar, NW China. *Gondwana Research* **19**, 958–74.

Zhang JE, Xiao WJ, Han CM, Mao QG, Ao SJ, Guo QQ and Ma C (2011b) A Devonian to Carboniferous intra-oceanic subduction system in Western Junggar, NW China. *Lithos* **125**, 592–606.

Zhang JE, Xiao WJ, Luo J, Chen YC, Windley BF, Song DF, Han CM and Safonova I (2018) Collision of the Tacheng block with the Mayile-Barleik-Tangbale accretionary complex in Western Junggar, NW China: implication for Early-Middle Paleozoic architecture of the western Altaids. *Journal of Asian Earth Sciences* **159**, 259–78.

Zhang HC and Zhu YF (2018) Geochronology and geochemistry of the Huilvshan gabbro in west Junggar (NW China): implications for magma process and tectonic regime. *Mineralogy and Petrology* **112**, 297–315.

Zhao ZH (2010) Trace element geochemistry of accessory minerals and its applications in petrogenesis and metallogenesis. *Earth Science Frontiers* **17**, 267–86 (in Chinese with English abstract).

Zhu YF, Chen B and Qiu T (2015) Geology and geochemistry of the Baijiantan-Baikouquan ophiolitic mélanges: implications for geological evolution of west Junggar, Xinjiang, NW China. *Geological Magazine* **152**, 41–69.